

Article

Mixed convection from an isothermal rough plate

Aubrey Jaffer^{1,*}, Martin Jaffer²¹ Independent Researcher, Waltham, MA 02452, USA² Independent Researcher, Atlanta, GA 30318, USA* Corresponding author: Aubrey Jaffer, agj@alum.mit.edu

CITATION

Jaffer A, Jaffer M. Mixed convection from an isothermal rough plate. *Thermal Science and Engineering*. 2025; 8(1): 9275.
<https://doi.org/10.24294/tse9275>

ARTICLE INFO

Received: 4 September 2024
Accepted: 16 December 2024
Available online: 23 January 2025

COPYRIGHT



Copyright © 2025 Author(s).
Thermal Science and Engineering is published by EnPress Publisher, LLC. This work is licensed under the Creative Commons Attribution (CC BY) license.
<https://creativecommons.org/licenses/by/4.0/>

Abstract: This investigation derives formulas to predict the mixed convective surface conductance of a flat isotropic surface roughness having a convex perimeter in a Newtonian fluid with a steady forced flow in the plane of that roughness. Heat transfer measurements of a 30.5 cm square rough plate with forced air velocities between 0.1 m/s and 2.5 m/s were made by the present apparatus in two inclined and all five orthogonal orientations. The present work's formulas are compared with 104 measurements in twelve data-sets. The twelve data-sets have root-mean-square relative error (RMSRE) values between 1.3% and 4% relative to the present theory. The present work's formulas are also compared with 78 measurements in 28 data-sets on five vertical rough surfaces in horizontal flow from prior work. The five stucco data-sets have RMSRE values between 2.5% and 6.5%; the other data-sets have RMSRE values between 0.2% and 5%.

Keywords: heat transfer; surface roughness; natural convection; forced flow

1. Introduction

Natural convection is the flow caused by nonuniform density in a fluid under the influence of gravity. Forced convection is the heat or solute transfer to or from a surface induced by forced fluid flow parallel to that surface. Mixed convection is the heat or solute transfer when both processes are operating simultaneously.

Modeling mixed convection from the exterior faces of walls and roofs is essential to predicting the thermal performance of buildings and determining their heating and cooling requirements. This investigation derives and tests mixed convection formulas for a rough, flat exterior face at any inclination, subjected to forced flow in the plane of the surface.

Three modes of forced flow of a Newtonian fluid along a (flat) surface are laminar flow, turbulent flow, and rough flow. Flow along flat, smooth plates gradually transitions from laminar to turbulent in a continuous boundary-layer¹ [1].

Surface roughness repeatedly disrupts the boundary-layer in rough flow, which occurs along rough surfaces [2].

Forced convection fluid flow is parallel to the surface. In natural convection the temperature difference between the fluid and surface creates an upward or downward fluid flow, which is not necessarily parallel to the surface. Along a vertical plate, "aiding" has natural and forced flows in the same direction; "opposing" flows are in opposite directions.

Natural convection is sensitive to plate inclination, while forced convection is not. Forced convection has different formulas for laminar, turbulent, and rough flows, while a single formula governs both laminar and turbulent natural convection [3–5].

There is a symmetry in external natural convection; a cooled plate induces downward flow instead of upward flow. Flow from a cooled upper face is the mirror image of flow from

a heated lower face. Flow from a cooled lower face is the mirror image of flow from a heated upper face.

The rest of this investigation assumes a surface warmer than the fluid.

1.1. Fluid mechanics

In engineering, heat transfer rates for both natural and forced convection are expressed using the average surface conductance \bar{h} with units $W/(m^2 \cdot K)$.

In fluid mechanics, the convective heat transfer rate is represented by the dimensionless average Nusselt number ($\overline{Nu} \equiv \bar{h} L/k$), where k is the fluid's thermal conductivity with units $W/(m \cdot K)$, and L is the system's characteristic length (m).

The Reynolds number Re is dimensionless and proportional to fluid velocity. The Rayleigh number Ra is the impetus for fluid flow due to temperature difference and gravity. A fluid's Prandtl number Pr is its momentum diffusivity per thermal diffusivity ratio. The system's characteristic length L scales both \overline{Nu} and Re ; Ra is scaled by L^3 ; both \bar{h} and Pr are independent of L .

1.2. Combining transfer processes

Equation (1) is an unnamed form for combining functions which appears frequently in heat transfer formulas:

$$F^p = F_1^p + F_2^p \tag{1}$$

Churchill and Usagi [6] stated that such formulas are “remarkably successful in correlating rates of transfer for processes which vary uniformly between these limiting cases.” Convection transfers heat (or solute) between the plate and fluid.

1.3. The ℓ^p -norm

When $F_1 \geq 0$ and $F_2 \geq 0$, taking the p th root of both sides of Equation (1) yields a vector-space functional form known as the ℓ^p -norm, which is notated $\|F_1, F_2\|_p$:

$$\|F_1, F_2\|_p \equiv [|F_1|^p + |F_2|^p]^{1/p} \tag{2}$$

Norms generalize the notion of distance. Formally, a vector-space norm obeys the triangle inequality: $\|F_1, F_2\|_p \leq |F_1| + |F_2|$, which holds only for $p \geq 1$. However, $p < 1$ is also useful.

- When $p > 1$, the processes modeled by F_1 and F_2 compete and $\|F_1, F_2\|_p \geq \max(|F_1|, |F_2|)$; the most competitive case is $\|F_1, F_2\|_{+\infty} \equiv \max(|F_1|, |F_2|)$.
 - Equation (25) uses the ℓ^3 -norm.
 - Equation (26) uses the $\ell^{\sqrt{3}}$ -norm.
- The ℓ^2 -norm is equivalent to root-sum-squared; it models perpendicular competitive processes.
 - Equations (21) and (23) use the ℓ^2 -norm.
- The ℓ^1 -norm models independent processes; $\|F_1, F_2\|_1 \equiv |F_1| + |F_2|$.
- When $0 < p < 1$, the processes cooperate and $\|F_1, F_2\|_p \geq |F_1| + |F_2|$.
 - Cooperation between conduction and flow-induced heat transfer manifests as the $\ell^{1/2}$ -norm in natural convection Equation (7).
- When $p < 0$, $\|F_1, F_2\|_p \leq \min(|F_1|, |F_2|)$, with the transition sharpness controlled by p ; the extreme case is $\|F_1, F_2\|_{-\infty} \equiv \min(|F_1|, |F_2|)$. Negative p can model a single flow through serial processes; the most restrictive process limits the flow.
 - Equation (18) uses the ℓ^{-4} -norm.
 - Equation (A4) uses the $\ell^{-\sqrt{1/3}}$ -norm.

1.4. Roughness

The present theory treats surface roughness as an elevation function $z(x, y)$ defined on an area A having a convex perimeter. Function $z(x, y)$ has only one value at each (x, y) coordinate; thus surfaces with tunnels and overhangs are disqualified, as are porous surfaces. The mean elevation \bar{z} and root-mean-squared (RMS) height-of-roughness $\varepsilon \ll L$ are:

$$\bar{z} = \frac{\int_A z \, dA}{\int_A dA} \quad (3)$$

$$\varepsilon = \sqrt{\frac{\int_A |z - \bar{z}|^2 \, dA}{\int_A dA}} \quad (4)$$

1.5. Prior work

Nearly all of the experimental prior works [7–13] concern smooth plates. The exception is Rowley et al. [14], the 1930 result of cooperative research between the University of Minnesota and the American Society of Heating and Ventilation Engineers. They measured mixed convection of 0.305 m square vertical plates in horizontal flow in a wind tunnel. They tested common rough exterior surfaces, specifically concrete, brick, stucco, and rough and smooth plaster.

Mixed convection measurements from the graphs in Rowley et al. [14] were captured by measuring the distance from each point to its graph's axes, then scaling to the graph's units using the "Engauge" software (version 12.1). **Table 1** lists the data-sets to be compared with the present theory, where θ is the angle of the plate from vertical and ψ is the angle of the forced flow from the zenith; $\psi = 90^\circ$ is horizontal.

1.6. Approaches

Rowley et al. [14] provided graphs for engineering use which cover both laminar and turbulent flows. It applies only to forced horizontal flow in the plane of a vertical plate. It lacked a roughness metric which would have allowed application to other types of rough surfaces. Unfortunately, forced convection from rough plates does not scale simply, being inversely proportional to $\log^2(L/\varepsilon)$.

The present work is primarily theoretical, combining the system-wide heat transfer derivations of natural and forced convections from Jaffer [5] and Jaffer [2], respectively. It applies to convex flat surfaces at any inclination having isotropic roughness with $0 < \varepsilon \ll L$ and forced flow parallel to the surface.

1.7. Not empirical

Empirical theories derive their coefficients from measurements, inheriting the uncertainties from those measurements. Theories developed from first principles derive their coefficients mathematically. For example, Incropera et al. [15] (p. 210) gives the thermal conductance of one face of a diameter D disk into a stationary, uniform medium having thermal conductivity k as exactly $8k/[\pi D]$ (units $W/(m^2 \cdot K)$). The present theory derives from first principles; it is not empirical. Each formula is tied to aspects of the plate geometry and orientation, fluid, and flow.

Table 1. Rowley et al. mixed convection data-sets.

Surface	θ	ψ	$Ra \geq$	$Ra \leq$	$Re \geq$	$Re \leq$	Count
smooth-plaster	0.0°	90.0°	2.8×10^6	1.1×10^7	7.9×10^4	8.3×10^4	2
smooth-plaster	0.0°	90.0°	3.1×10^6	1.1×10^7	6.7×10^4	7.1×10^4	2
smooth-plaster	0.0°	90.0°	3.2×10^6	1.1×10^7	5.6×10^4	5.9×10^4	2
smooth-plaster	0.0°	90.0°	3.7×10^6	1.1×10^7	4.5×10^4	4.7×10^4	2
smooth-plaster	0.0°	90.0°	4.1×10^6	1.2×10^7	3.4×10^4	3.5×10^4	2
smooth-plaster	0.0°	90.0°	5.0×10^6	1.2×10^7	2.2×10^4	2.3×10^4	2
concrete	0.0°	90.0°	1.1×10^7	1.1×10^7	7.9×10^4	7.9×10^4	1
concrete	0.0°	90.0°	7.9×10^6	1.1×10^7	6.7×10^4	6.9×10^4	3
concrete	0.0°	90.0°	2.9×10^6	1.1×10^7	5.6×10^4	5.9×10^4	7
concrete	0.0°	90.0°	3.1×10^6	1.1×10^7	4.5×10^4	4.7×10^4	2
concrete	0.0°	90.0°	3.9×10^6	1.1×10^7	3.4×10^4	3.5×10^4	2
concrete	0.0°	90.0°	4.3×10^6	1.2×10^7	2.2×10^4	2.4×10^4	2
brick	0.0°	90.0°	2.0×10^6	1.1×10^7	6.4×10^4	6.7×10^4	6
brick	0.0°	90.0°	3.4×10^6	1.1×10^7	5.5×10^4	5.8×10^4	4
brick	0.0°	90.0°	2.7×10^6	1.1×10^7	4.5×10^4	4.7×10^4	3
brick	0.0°	90.0°	3.1×10^6	1.1×10^7	4.0×10^4	4.2×10^4	5
brick	0.0°	90.0°	4.3×10^6	1.1×10^7	3.0×10^4	3.2×10^4	4
brick	0.0°	90.0°	5.3×10^6	1.1×10^7	1.7×10^4	1.8×10^4	4
rough-plaster	0.0°	90.0°	1.1×10^7	1.1×10^7	6.7×10^4	6.7×10^4	1
rough-plaster	0.0°	90.0°	3.6×10^6	1.1×10^7	5.6×10^4	5.9×10^4	2
rough-plaster	0.0°	90.0°	3.7×10^6	1.1×10^7	4.5×10^4	4.7×10^4	2
rough-plaster	0.0°	90.0°	4.0×10^6	1.2×10^7	3.4×10^4	3.5×10^4	3
rough-plaster	0.0°	90.0°	4.8×10^6	1.2×10^7	2.2×10^4	2.4×10^4	2
stucco	0.0°	90.0°	1.1×10^6	1.1×10^7	6.7×10^4	7.1×10^4	2
stucco	0.0°	90.0°	6.9×10^5	1.1×10^7	5.6×10^4	6.0×10^4	3
stucco	0.0°	90.0°	1.2×10^6	1.1×10^7	4.5×10^4	4.8×10^4	3
stucco	0.0°	90.0°	1.5×10^6	1.1×10^7	3.4×10^4	3.6×10^4	3
stucco	0.0°	90.0°	2.1×10^6	1.1×10^7	2.2×10^4	2.4×10^4	2

1.8. RMS relative error

Root-mean-squared (RMS) relative error (RMSRE) provides an objective, quantitative evaluation of experimental data versus theory. It gauges the fit of measurements $g(Re_j)$ to function $f(Re_j)$, giving each of the n samples equal weight in Equation (5). Along with presenting RMSRE, charts in the present work split RMSRE into the bias and scatter components defined in Equation (6). The root-sum-squared of bias and scatter is RMSRE.

$$\text{RMSRE} = \sqrt{\frac{1}{n} \sum_{j=1}^n \left| \frac{g(Re_j)}{f(Re_j)} - 1 \right|^2} \tag{5}$$

$$\text{bias} = \frac{1}{n} \sum_{j=1}^n \left\{ \frac{g(Re_j)}{f(Re_j)} - 1 \right\} \quad \text{scatter} = \sqrt{\frac{1}{n} \sum_{j=1}^n \left| \frac{g(Re_j)}{f(Re_j)} - 1 - \text{bias} \right|^2} \tag{6}$$

2. Natural convection

Jaffer [5] derived a natural convection formula for external flat plates (with convex perimeter) in any orientation from its analyses of horizontal and vertical plates. This investigation uses the same approach.

Figure 1a–c show the induced fluid flows around heated vertical and horizontal surfaces.

For a horizontal plate with heated upper face, streamlines photographs in Fujii and Imura [3] show natural convection pulling fluid horizontally from above the plate's perimeter into a rising central plume. **Figure 1b** is a diagram of this upward-facing convection. Horizontal flow is nearly absent at the elevation of the dashed line.

The streamlines photograph of a vertical plate in Fujii and Imura [3] shows fluid being pulled horizontally before rising into a plume along the vertical plate. **Figure 1a** is its diagram.

Modeled on a streamlines photograph in Aihara et al. [16], **Figure 1c** is a flow diagram for a horizontal plate with heated lower face. Unheated fluid below the plate flows horizontally inward. It rises a short distance, flows outward closely below the plate, and flows upward upon reaching the plate edge. The edge flows self-organize so that they are at the opposing edges of the plate which are nearest to each other.

Horizontal flow in **Figure 1b** is radial, but not radial in **Figure 1c**.

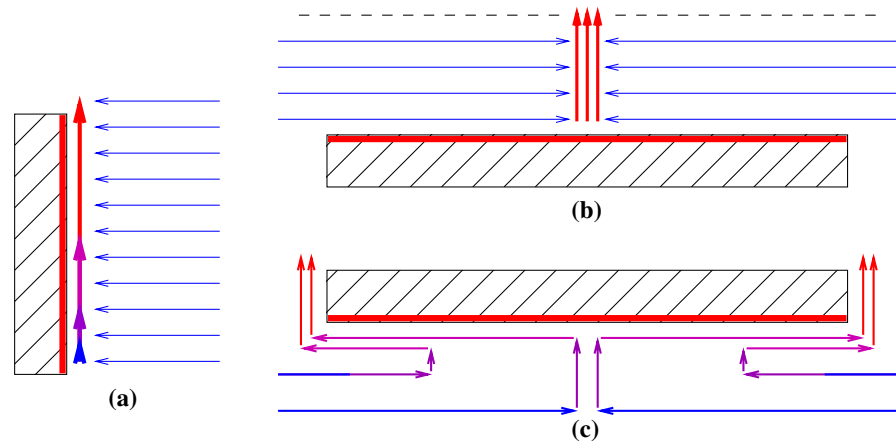


Figure 1. (a) Vertical plate, (b) flow above a heated plate, and (c) flow below a heated plate.

An important aspect of all three flow topologies is that fluid is pulled horizontally before being heated by the plate. Pulling horizontally expends less energy than pulling vertically because the latter does work against the gravitational force. Inadequate horizontal (or vertical) clearance around a plate can obstruct flow and reduce convection and heat transfer; such a plate is not “external”.

From thermodynamic constraints, Jaffer [5] derives generalized natural convection Equation (7) with the parameters specified in **Table 2**:

- θ is the angle of the plate from vertical;
- L is the characteristic length of a flat plate with convex perimeter:
 - face up L^* is the area-to-perimeter ratio;
 - vertical L' is the harmonic mean of the perimeter vertical spans (the height of a level rectangle);
 - face down L_R is the harmonic mean of the perimeter distances to that bisector which is perpendicular to the shortest bisector ($1/2$ of the shorter side of a rectangle);
- Nu_0 is the conduction into the fluid when not moving (static);

- Ra' is computed with vertical L' ; $Ra^* = Ra' [L^*/L']^3$; $Ra_R = Ra' [L_R/L']^3$.
 Pr does not affect upward-facing heat transfer because the heated fluid flows directly upward, as does conducted heat. When heated fluid must flow along vertical and downward-facing plates, its heat transfer potential is reduced by dividing Ra by Ξ from Equation (8).
- E is the count of 90° changes in direction of fluid flow;
- B is the sum of the mean lengths of flows parallel to the plate divided by L ;
- C is the plate area fraction responsible for flow induced heat transfer;
- D is the effective length of heat transfer contact with the plate divided by L ;
- The ℓ^p -norm combines the static conduction and induced convective heat flows.

$$\overline{Nu} = \left\| Nu_0 [1 - C], {}^{2+E}\sqrt{[C D Nu_0]^{3+E} \frac{2}{B} Ra} \right\|_p \quad (7)$$

$$\Xi = \left\| 1, \frac{0.5}{Pr} \right\|_{\sqrt{1/3}} \quad Nu_0^* = \frac{2}{\pi} \quad Nu_0' = \frac{2^4}{\sqrt{2} \pi^2} \quad (8)$$

Table 2. Natural convection parameters.

Face	θ	L	\overline{Nu}	Nu_0	Ra	E	B	C	D	p
up	-90°	L^*	\overline{Nu}^*	Nu_0^*	Ra^*	1	2	$1/\sqrt{8}$	1	1/2
vertical	0°	L'	\overline{Nu}'	Nu_0'	Ra'/Ξ	1	1/2	1/2	1/4	1/2
down	$+90^\circ$	L_R	\overline{Nu}_R	$Nu_0'/2$	Ra_R/Ξ	3	4	1/2	2	1

2.1. Effective vertical reynolds number

From the derivation in Jaffer [5] with $Ra'/\Xi \gg 1$, $\overline{Nu} \approx C D Nu_0 Re$. Heat transfer \overline{Nu}' is reduced by the self-obstruction factor $1/\sqrt[3]{\Xi}$, which grows with Pr . However, heat transfer is not the same as fluid flow, which increases with decreasing Pr . The Ξ^3 factor in Equation (9) makes Re_N increase with decreasing Pr . Proposed is Equation (9) as the Reynolds number associated with the natural convective flow from a vertical plate.

$$Re_N \approx \frac{\overline{Nu} \Xi^{2+E}}{Nu_0 C D} = \frac{8 \overline{Nu}' \Xi^3}{Nu_0'} \quad \overline{Nu}' \gg Nu_0' \quad (9)$$

2.2. Natural convection from an inclined plate

Ra is proportional to gravitational acceleration. Following the approach of Fujii and Imura [3], the Ra argument to $\overline{h}'(Ra) \equiv k \overline{Nu}'(Ra)/L'$ is scaled by $|\cos \theta|$, modeling the reduced convection of a tilted plate as a reduction in gravitational acceleration. Similarly, the Ra arguments to \overline{h}^* and \overline{h}_R are scaled by $|\sin \theta|$. An unobstructed plate induces a single steady-state mode of natural convection (face up, down, or vertical). The instances of $\max()$ in Equation (10) choose the largest surface conductance among these modes.

$$\overline{h} = \begin{cases} \max(\overline{h}'(|\cos \theta| Ra'/\Xi), \overline{h}^*(|\sin \theta| Ra^*)) & \sin \theta < 0 \\ \max(\overline{h}'(|\cos \theta| Ra'/\Xi), \overline{h}_R(|\sin \theta| Ra_R/\Xi)) & \sin \theta \geq 0 \end{cases} \quad (10)$$

In reality, the θ transition is more gradual using the ℓ^{16} -norm in Equation (11):

$$\bar{h} = \begin{cases} \|\bar{h}'(|\cos \theta| Ra' / \Xi), \bar{h}^*(|\sin \theta| Ra^*)\|_{16} & \sin \theta < 0 \\ \|\bar{h}'(|\cos \theta| Ra' / \Xi), \bar{h}_R(|\sin \theta| Ra_R / \Xi)\|_{16} & \sin \theta \geq 0 \end{cases} \quad (11)$$

2.3. Rough natural convection

The agreement of rough plate measurements with theory over the $\pm 90^\circ$ range in **Figure 2** indicates that Equation (11) governs plates with RMS height-of-roughness $0 \leq \varepsilon \ll L$.

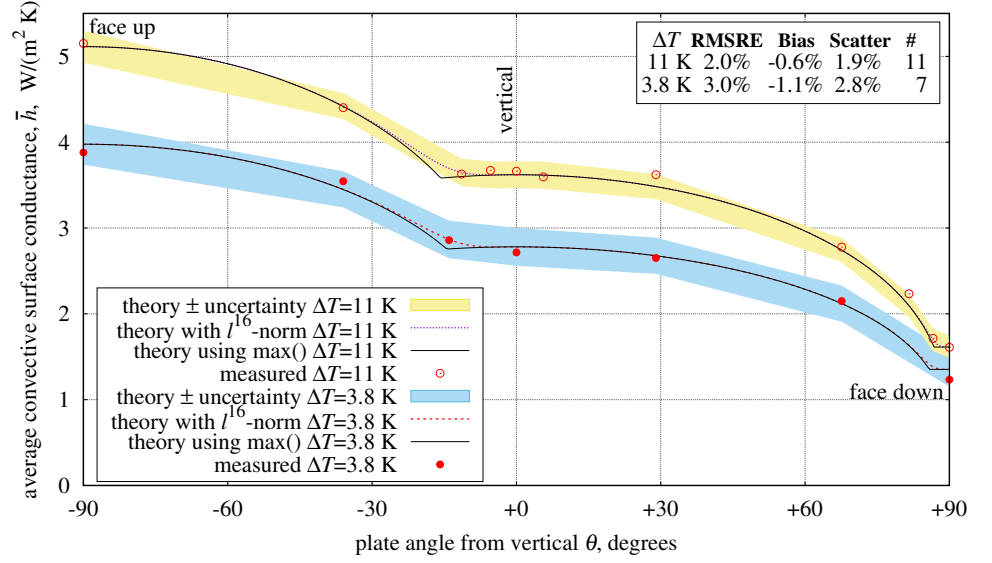


Figure 2. Rough $\varepsilon = 3.0$ mm natural convection versus angle.

3. Forced convection

Forced convection \overline{Nu} is the heat transfer caused by forced flow along (and parallel to) a heated plate. The surface conductance $\overline{h}_F \equiv \overline{Nu} k / L$ grows with Re_F , Pr , and k . Its characteristic length L is the length of the plate in the direction of forced flow.

3.1. Rough convection

Jaffer [2] derives the forced convection \overline{Nu}_ρ of rough flow from isotropic, periodic roughness:

$$\overline{Nu}_\rho(Re_F) = \frac{Re_F Pr_\infty^{1/3} w}{6 [\ln(L/\varepsilon)]^2} \quad Re_F > \left[\frac{0.664}{\varepsilon} \right]^2 L_P L \quad (12)$$

$$w = \|1, \varepsilon/L_W\|_{\sqrt{1/2}} \quad (13)$$

- $\varepsilon \ll L$ is the root-mean-squared (RMS) height of roughness.
- $L_P \ll L$ is the isotropic period of the roughness [2].
- L_W is the width of the plate (perpendicular to L).
- Pr_∞ is the bulk fluid's Prandtl number (far from the plate).

If the roughness extends to the plate's rim, then it increases the effective width of the rough face by more than 2ε because, in addition to the fluid adjacent to plate's face and rim, the fluid near the edge between them is affected. Thus ε and plate width L_W cooperate weakly, leading to an effective width of $\|L_W, \varepsilon\|_{\sqrt{1/2}}$. Dividing by L_W , Equation (13) is the edge roughness correction factor w . **Figure 3** graphs w as a function of ε .

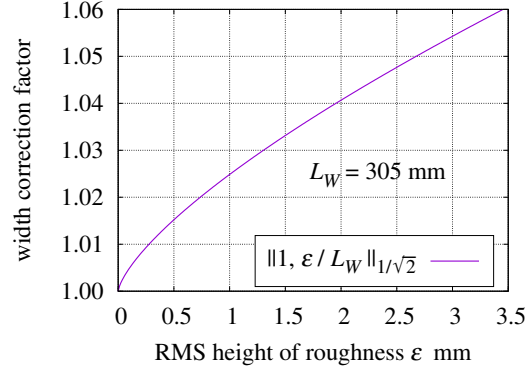


Figure 3. Edge roughness correction factor.

3.2. Plateau roughness

There are isotropic, periodic roughnesses whose convective heat transfer differs from Equation (12).

- Informally, a “plateau roughness” is an isotropic, periodic roughness with most of its area at its peak elevation. A quantitative definition is given in Jaffer [2].
- A “plateau wells roughness” is an array of co-planar wells dropping below a flat surface.
- A “plateau islands roughness” is an array of co-planar islands.

The present apparatus plate has plateau islands roughness.

For a given Re_F , a plateau roughness may contain areas transferring heat per Equation (12), and separate areas transferring heat as turbulent flow along a smooth plate, but with characteristic length L_P .

3.3. Turbulent forced convection

Jaffer [2] derives the average surface conductance, $\overline{h_F} \equiv \overline{Nu_\tau} k/L$, of turbulent flow along an isothermal plate as Equation (14).

$$\overline{Nu_\tau} = \frac{Nu_0 Re_F \overline{f_\tau}}{\sqrt{3}} \sqrt{\frac{Pr/\sqrt{162} + 1}{\sqrt{162} Pr \overline{f_\tau} + 1}} \sqrt[3]{\frac{Pr/\Xi}{\|1, 1/Pr\|_3}} \quad \sqrt{162} \equiv 9\sqrt{2} \quad (14)$$

$$\overline{f_\tau} = \frac{2^{-5/4}}{[W_0(Re_F/\sqrt{3}) - 1]^2} \quad \Xi = \left\| 1, \frac{0.5}{Pr} \right\|_{\sqrt{1/3}} \quad Nu_0 = \frac{2^4}{\pi^2 \sqrt[4]{2}} \quad (15)$$

- The fluid’s effective Prandtl number $Pr = Pr_W^{1/4} Pr_\infty^{3/4}$ (from Žukauskas and Šlančiauskas [17]).
 Pr_W is the Prandtl number of fluid at wall (plate) temperature.
 Pr_∞ is the Prandtl number of fluid at the bulk flow temperature.
- W_0 is the principal branch of the Lambert W function, defined as $W_0(\varphi \exp \varphi) = \varphi$ when $\varphi \geq 0$.
- In Equation (15), $2^{-5/4}$ replaces the $\sqrt[3]{2}/3$ coefficient from Jaffer [2], a +0.11% correction.
- Plateau islands roughness can shed rough and turbulent flow simultaneously.

3.4. Plateau islands roughness

The plateau islands roughness described in Appendix C has $\overline{Nu_\rho}$ Equation (12) rough convection in the leading Re_I/Re_F portion of the plate, and $\overline{Nu_I}$ Equation (16) turbulent convection in the rest of the plate. Equation (17) Re_I separates the regions, where L^\bullet is the ratio of each (convex) island’s area to its perimeter.

$$\overline{Nu}_I = \left\{ 1 - \Omega + \left\| \frac{\Omega}{2}, \frac{2\varepsilon [4L^\bullet]}{L_P^2} \right\|_2 \right\} \frac{L}{L_P} \overline{Nu}_r \left(\frac{Re_F L_P}{L} \right) \quad (16)$$

$$Re_I = \frac{3^3 \varepsilon^2 L^2}{L^\bullet L_P^3} \ln \frac{3^3 \varepsilon^2 L^2}{\sqrt{3} L^\bullet L_P^3} \quad (17)$$

$$\overline{Nu}_i = \overline{Nu}_I(Re_F) + \overline{Nu}_\rho(\|Re_F, Re_I\|_{-4}) - \overline{Nu}_I(\|Re_F, Re_I\|_{-4}) \quad (18)$$

“Openness” $0 < \Omega < 1$ is the non-plateau area per cell area ratio. Given a $w \times w$ matrix of elevations $S_{s,t}$:

$$\Omega \approx \frac{1}{w^2} \sum_{t=0}^{w-1} \sum_{s=0}^{w-1} \begin{cases} 1, & S_{s,t} < \max(S) - \varepsilon^2/L_P \\ 0, & \text{otherwise} \end{cases} \quad (19)$$

In the log-log plots in **Figure 4a,b**, the effective Re_F exponent is the slope of its line. For example, the “ $Re_F/200$ ” and “ $Re_F/333$ ” lines have slope 1; thus they are proportional to $Re_F^1 \equiv Re_F$. In each plot, the “bi-level” trace is \overline{Nu}_i Equation (18). The “turbulent part” trace is Equation (20), which is the turbulent component of \overline{Nu}_i Equation (18):

$$\overline{Nu}_I(Re_F) - \overline{Nu}_I(\|Re_F, Re_I\|_{-4}) \quad (20)$$

In both **Figure 4a,b**, the slope of the Equation (20) “turbulent part” trace is close to 1 through more than an order of magnitude of Re_F . The discrepancy at larger Re_F is unimportant because the heat transfer is dominated by forced convection in that range.

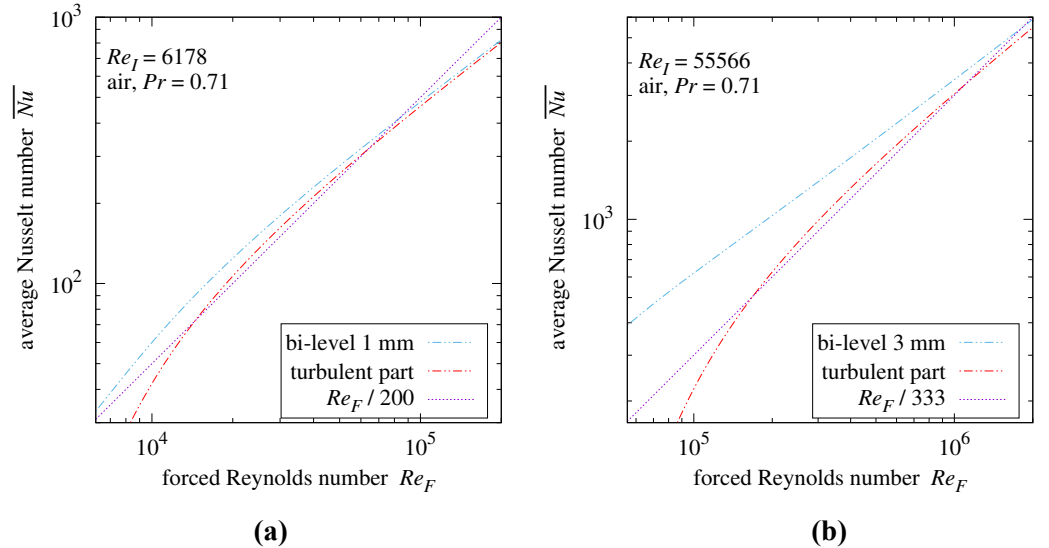


Figure 4. (a) Forced convection $Re_I = 6178$ and (b) Forced convection $Re_I = 55,566$.

4. Mixing natural and forced convections

The previous sections established that:

- The effective natural Reynolds number Re_N is proportional to \overline{Nu}_N when $\overline{Nu}_N \gg Nu_0$.
- Forced rough convection \overline{Nu}_ρ is proportional to Re_F in Equation (12).
- And forced turbulent Equation (20) is nearly proportional to Re_F when $Re_F > Re_I$.

On that basis, this investigation proposes:

- Surface conductances \overline{h}_N and \overline{h}_F both being proportional to Reynolds numbers indicates that they are commensurate; they can be combined using symmetrical functions such as the ℓ^p -norm.

One approach to predicting mixed convection would be to compute \overline{Nu} from a function of Re_F and Re_N . However, choosing a single \overline{Nu} formula is problematic; while Re and \overline{Nu} are nearly proportional in all three cases, their coefficients are very different. Also, rough convection \overline{Nu}_ρ is strongly dependent on height-of-roughness ε , but Section 2 found that natural convection is insensitive to roughness $\varepsilon \ll L$.

- This investigation combines a natural surface conductance \overline{h}_N (specifically \overline{h}^* , \overline{h}' , or \overline{h}_R) with the forced surface conductance \overline{h}_F using the ℓ^p -norm (where p depends on plate and flow orientations). Surface conductance \overline{h} is used instead of \overline{Nu} in order to avoid characteristic-length mismatch between \overline{Nu} formulas.

This approach departs from prior works (all of which concerned smooth plates), which compute \overline{Nu} from a ratio of powers of Re_F and the Grashof number $Gr = Ra/Pr$.

4.1. Theory and measurements

Figures which follow plot \overline{Nu} at $L = L'$ measurements and theoretical curves versus $10^3 < Re_F < 10^5$ using logarithmic scales on both axes. Logarithmic scales do not include 0; the following figures plot the natural convection measurement ($Re_F = 0$) at $Re_F = 10^3$.

θ is the angle of the plate from vertical; -90° is face up; $+90^\circ$ is face down.

ψ is the angle of the forced flow from the zenith; $\psi = 90^\circ$ is horizontal flow; $\psi = 0^\circ$ is upward. In this investigation, forced flow is always parallel to the plate; hence, horizontal plates have $\psi = 90^\circ$.

RMSRE is calculated from the measurements between the vertical lines, $1950 < Re_F < 5 \times 10^4$.

The $\varepsilon = 3$ mm plate sheds only rough flow at $1950 < Re_F < 5 \times 10^4$; its graphs are captioned “rough”. The $\varepsilon = 1.04$ mm plate sheds rough flow at $Re_F < Re_I = 6178$ and turbulent flow otherwise. Hence it sheds mostly turbulent flow at $1950 < Re_F < 5 \times 10^4$; its graphs are captioned “turbulent”.

5. Horizontal forced flow

5.1. Vertical plate with horizontal forced flow

Figure 1a shows that fluid is drawn horizontally towards the heated surface, then rising. The forced and natural heat flows are thus perpendicular, suggesting the ℓ^2 -norm for combining \overline{h}_F and vertical \overline{h}' :

$$\overline{h} = \|\overline{h}_F, \overline{h}'\|_2 \quad (21)$$

5.2. American society of heating and ventilation engineers

Rowley et al. [14] measured mixed convection of 0.305 m square vertical plates in horizontal flow in a wind tunnel. Their graphs report surface conductance of the plate versus T_m , the mean of the plate and airflow (Fahrenheit) temperatures. The Rayleigh numbers used by natural convection formulas have the temperature difference as a factor. Through trial and error it was found that taking $1.05 T_m$ as the (Fahrenheit) plate temperature and $0.95 T_m$ as the fluid temperature kept RMSRE values less than 10%, which fixed temperature offsets did not. Using coefficients of 1.1 and 0.9 or 1.2 and 0.8 did not strongly affect RMSRE values.

Figures 5 and 6 compare ($\overline{Nu} \equiv \overline{h} L/k$) Equation (21) with measurements of vertical plates in horizontal flow shedding turbulent and rough flow, respectively.

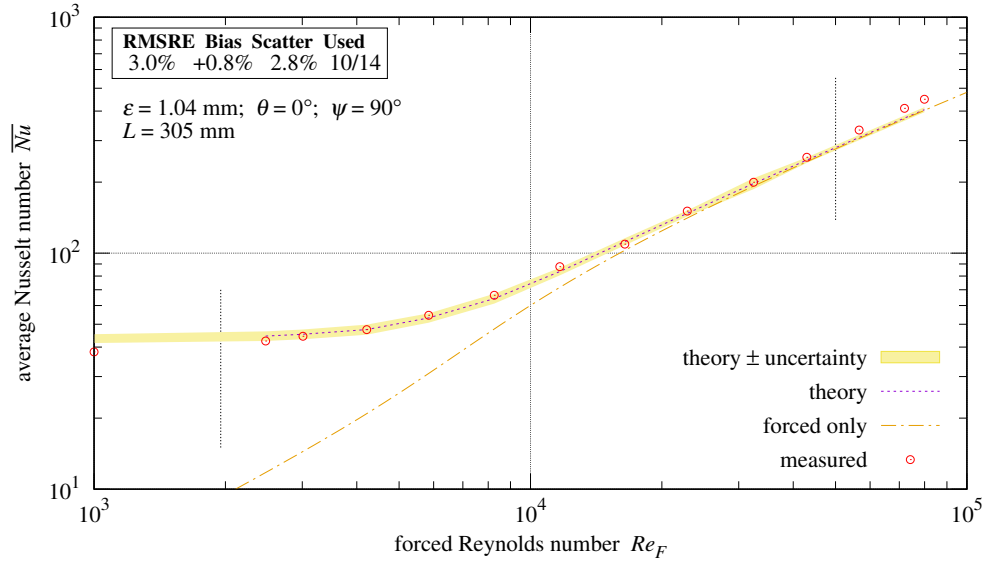


Figure 5. Vertical plate in horizontal forced turbulent flow.

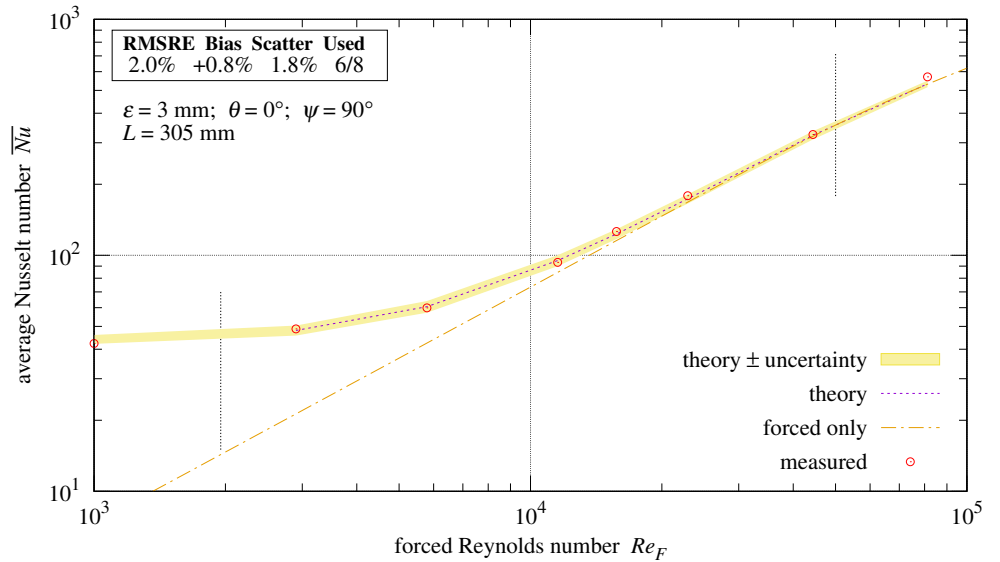


Figure 6. Vertical plate in horizontal forced rough flow.

At a constant rate of airflow, increasing fluid temperature causes kinematic viscosity ν to grow and h_F to shrink because $Re_F = V L/\nu$. However, the traces in the graphs from Rowley et al. [14] show increasing convective conductance with temperature. Rowley et al. [14] reports the airspeed measured at the center of the duct (of which the rough plate replaces one side). However, V is defined as the average velocity inside a duct. Let V_\odot be the velocity at the center of the duct.

The velocity is 0 at the duct wall, so some velocity near the wall must be used as the effective velocity V at the test plate. The velocity profile across the duct develops from flat at the duct entrance to the Hagen-Poiseuille parabolic velocity profile for a “fully developed” flow [18] (p. 356). The dimensionless development length is $L_D/D = 25.625$, where $L_D = 5.207 \text{ m}$ is the duct length between the fan and the leading edge of the plate and $D = 203.2 \text{ mm}$ is the hydraulic-diameter of the duct.

$V = V_\odot$ when $L_D = 0$; otherwise $V < V_\odot$. Dimensional analysis finds that V must depend on $V_\odot, L_D/D, \nu$, and a viscosity parameter which is independent of temperature. For a gas, let ν_0 be the viscosity at its boiling point.

Dry air is composed of 78.084% N₂, 20.946% O₂, and 0.934% Argon. N₂ has kinematic viscosity $\nu_0 = 1.15 \times 10^{-6} \text{ m}^2/\text{s}$ at its 77.355 K boiling point. O₂ has $\nu_0 = 1.58 \times 10^{-6} \text{ m}^2/\text{s}$ at its 90.188 K boiling point; Argon gas has $1.4223 \times 10^{-6} \text{ m}^2/\text{s}$ at 100 K. Combining these per the air percentages yields $\bar{\nu}_0 = 1.2422 \times 10^{-6} \text{ m}^2/\text{s}$. Equation (22) is the effective V at the plate.

$$V = V_{\odot} / \left[1 + \sqrt{2} \frac{L_D}{D} \frac{\bar{\nu}_0}{\nu} \right] \quad \bar{\nu}_0 \approx 1.2422 \times 10^{-6} \frac{\text{m}^2}{\text{s}} \quad (22)$$

Rowley et al. [14] did not characterize the roughnesses other than to note that the forced convection component was greatest from stucco, followed by brick and rough-plaster, followed by concrete, and the least from smooth-plaster. This investigation has assigned the RMS height-of-roughness (ϵ) parameters shown in **Table 3**.

Table 3. Assigned parameters.

Figure	Surface	ϵ	ϵ
Figure 7	stucco	0.91	1.47 mm
Figure 8a	rough-plaster	0.91	0.75 mm
Figure 8b	brick	0.93	0.75 mm
Figure 9a	concrete	0.94	0.55 mm
Figure 9b	smooth-plaster	0.91	0.20 mm

Rowley et al. [14] did not address thermal radiative transfers except to state “In order to obtain average radiation conditions, the inside surface of the test duct was painted a dull gray, and all the pipe outside of the refrigerator was covered with a one-inch thick blanket of insulating material.” **Table 3** shows common values for the surface emissivity ϵ of each rough material tested. Experimenting with its value, an effective inside surface emissivity of $\epsilon = 0.70$ keeps all non-stucco RMSRE values less than 5%. Unexpectedly small for paint, $\epsilon = 0.70$ would compensate for the wind-tunnel walls being warmer than the forced airflow.

Figure 7 shows the mixed convective conductance curves for stucco, the roughest surface Rowley et al. [14] tested. The derivation in Jaffer [2] of rough convection Equation (12) assumes isotropic roughness. Stucco being non-uniform in its application, it has larger RMSRE than the other surfaces.

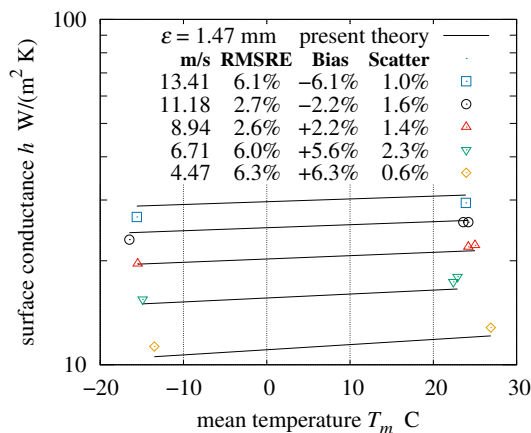


Figure 7. Stucco.

Figures 8a,b and **9a,b** compare the present theory with measurements from rough plaster, brick, concrete, and smooth plaster, respectively². Closer to the isotropic ideal, they have RMSRE values smaller than 5%.

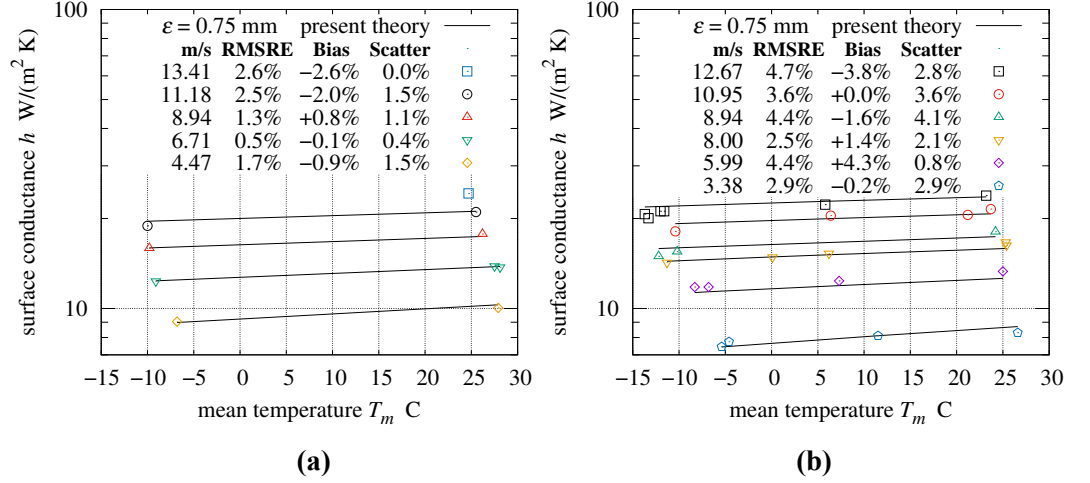


Figure 8. (a) Rough Plaster and (b) Brick.

Lacking the actual RMS height-of-roughness and emissivities of the original apparatus, while these results lend support to the present theory, they are not conclusive.

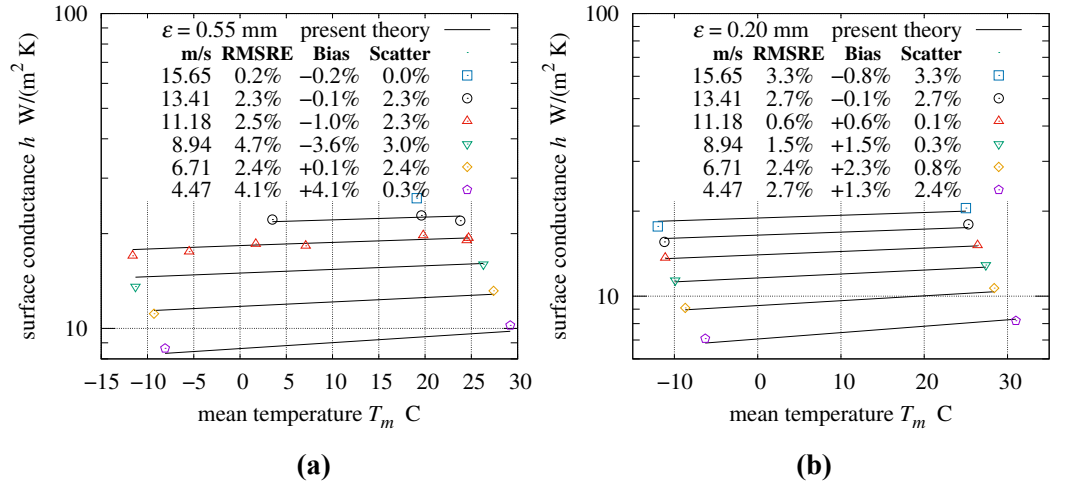


Figure 9. (a) Concrete and (b) Smooth plaster.

5.3. Upward facing plate

Figure 1b shows that flow is inward above the heated surface. Forced flow parallel to the surface is thus compatible with upward natural convection \bar{h}^* . Their heat flows are perpendicular, suggesting the ℓ^2 -norm for combining \bar{h}^* and \bar{h}_F :

$$\bar{h} = \|\bar{h}_F, \bar{h}^*\|_2 \quad (23)$$

Figures 10 and **11** compare Equation (23) with measurements of upward-facing plates shedding turbulent or rough flow, respectively.

5.4. Downward facing plate

Figure 1c shows that flow is outward immediately beneath the heated surface. Forced flow parallel to this surface is thus incompatible with downward natural convection \bar{h}_R . These two fluid flows will compete for surface area. **Table 2** shows that \bar{Nu}_R is asymptotically proportional to $\sqrt[5]{Ra_R}$. The ℓ^5 -norm combines Ra_R with Re_F^5 , manifesting the fragility of

\bar{h}_R flow because moderate Re_F values can overpower the \bar{h}_R term:

$$\bar{h} = \|\bar{h}_F, \bar{h}_R\|_5 \tag{24}$$

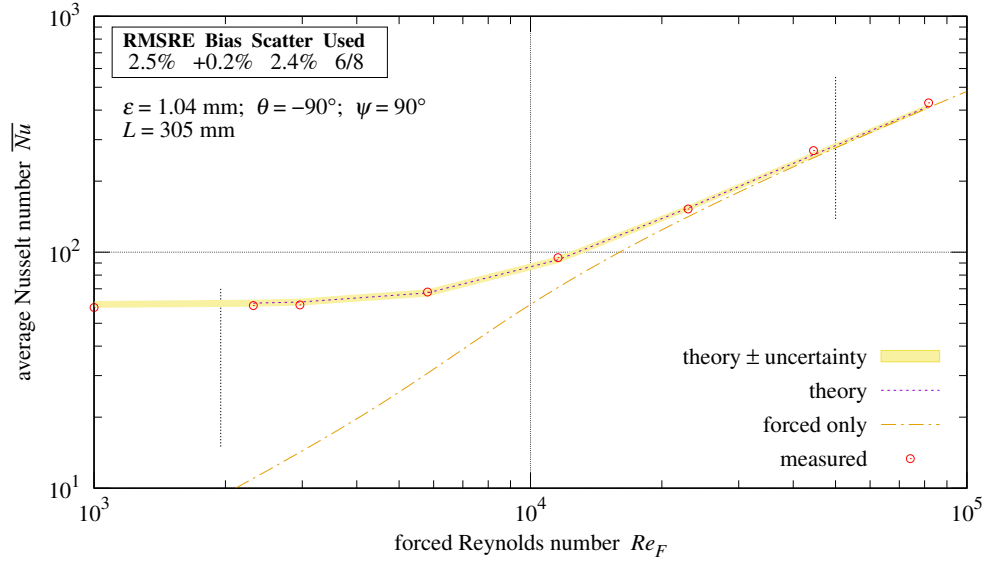


Figure 10. Upward facing plate in horizontal forced turbulent flow.

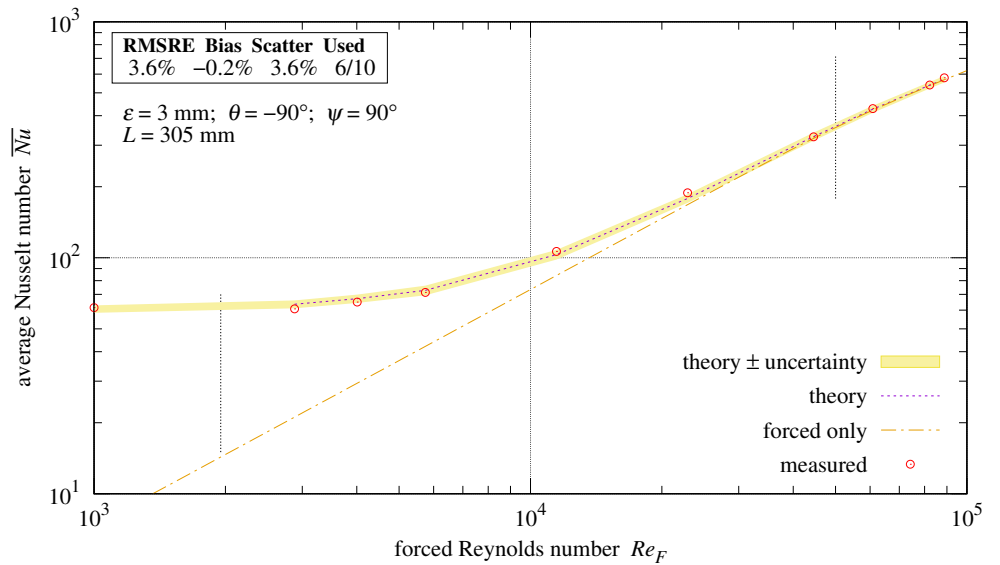


Figure 11. Upward facing plate in horizontal forced rough flow.

Figures 12 and 13 compare Equation (24) with measurements of downward-facing plates shedding turbulent or rough flow, respectively.

6. Vertical plate with vertical forced flow

A vertical plate with vertical forced flow requires a more thorough analysis.

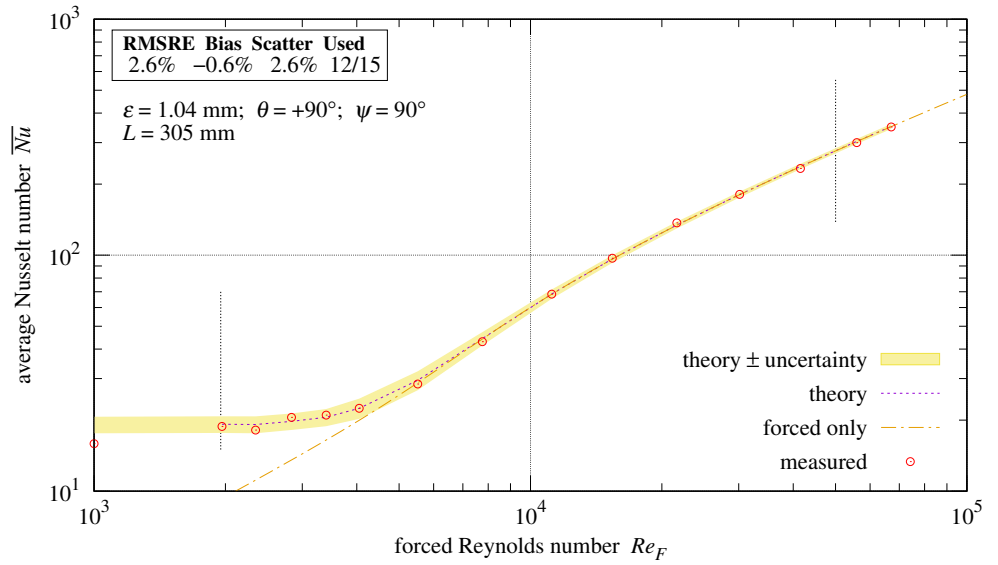


Figure 12. Downward facing plate in horizontal forced turbulent flow.

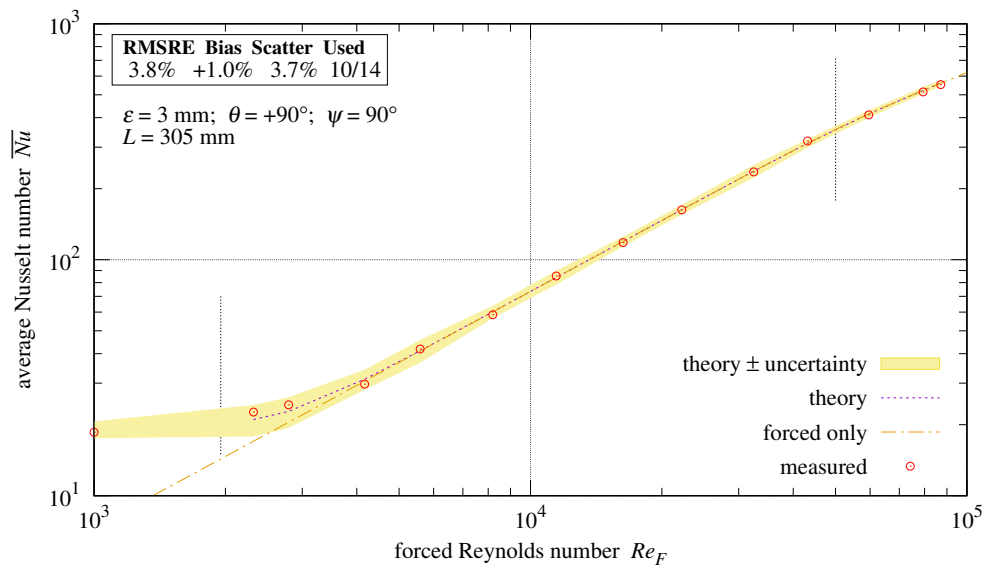


Figure 13. Downward facing plate in horizontal forced rough flow.

6.1. Velocity profiles

The velocity profile function $u(y)$ is the velocity at $x = L/2$ and distance $0 < y < \delta$ from the plate, where δ is the boundary layer thickness at $x = L/2$. Positive $u(y)$ is in the direction of forced flow. The upper plot in **Figure 14** shows the velocity profiles of forced turbulent and natural convection adjacent to a vertical 30.5 cm square plate per the theory in Appendix A, as well as their sum and difference profiles.

The widest y span of constant $u(y)$ occurs in opposing vertical flows when $Re_F = Re_N$. Because of the laminar sublayer of turbulent flows, this cancellation occurs around $u = 0.065$ m/s, not $u = 0$.

The lower plot in **Figure 14** shows the theoretical velocity profiles of forced turbulent flow, and that flow combined with laminar natural flow. The forced Re_F values are double and half of natural Re_N .

In the opposing flow cases, the “forced – natural” and “forced – natural 21,600” traces both have two inflection points near the plate. These indicate that the boundary layer is split,

with laminar flow at $0 < y < 5$ mm and turbulent flow at $5 < y < 15$ mm.

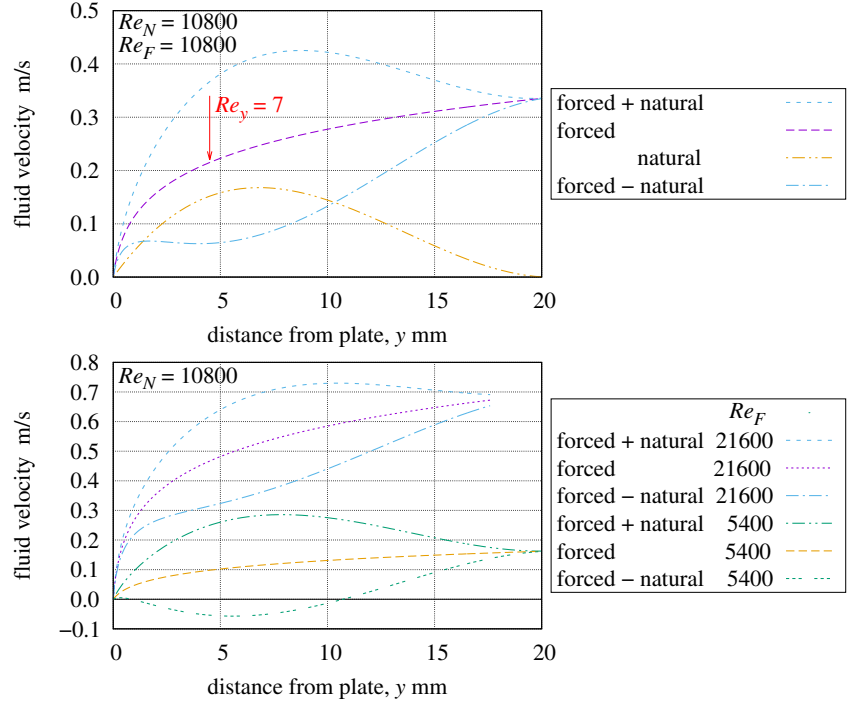


Figure 14. Velocity profiles.

6.2. Vertical plate with forced downward flow

Because the net velocity of the “forced – natural 5400” curve goes negative near the plate, these opposing fluid flows compete for plate area. $\overline{Nu'}$ is asymptotically proportional to $\sqrt[3]{Ra'}$ in **Table 2**; the ℓ^3 -norm combines Ra' with Re_F^3 (which is more robust than the ℓ^5 -norm):

$$\bar{h} = \|\overline{h_F}, \overline{h'}\|_3 \quad (25)$$

The “forced – natural 21,600” trace indicates that its boundary layer is split with laminar natural flow near the plate and forced turbulent flow away. This serves to increase heat transport through the boundary layer (compared with pure laminar), exceeding the ℓ^2 -norm, but less than the $\ell^{\sqrt{2}}$ -norm. The “mixed $\ell^{\sqrt{3}}$ -norm” curve, Equation (26), is close to the upper measurements in **Figures 15** and **16**.

$$\bar{h} = \|\overline{h_F}, \overline{h'}\|_{\sqrt{3}} \quad (26)$$

Both the 1 mm and 3 mm plates had plateau islands roughness, as described in Section 3. The Re_I arrow marks the transition from rough to turbulent flow along the plateau islands roughness.

The Re_N arrow indicates the position of natural convection’s effective Reynolds number calculated by Equation (9). “ $Re_N \chi_I$ ” is Re_N scaled by the roughness correction ($\chi_I \geq 1$) detailed in Appendix B; it marks the Re_F lower-bound of the transition between $p = 3$ and $p = \sqrt{3}$.

When the whole plate is shedding turbulent flow, $\chi_I = 1$. When the whole plate is shedding rough flow, $\chi_I = \chi$, which is derived in Appendix A. The close spacing between the arrows in **Figure 15** indicates that nearly all of the plate is shedding turbulent flow.

Figures 15 and **16** show the theory curve and the measurements switching from the “mixed ℓ^3 -norm” to the “mixed $\ell^{\sqrt{3}}$ -norm” at $Re_F > Re_N \chi_I$.

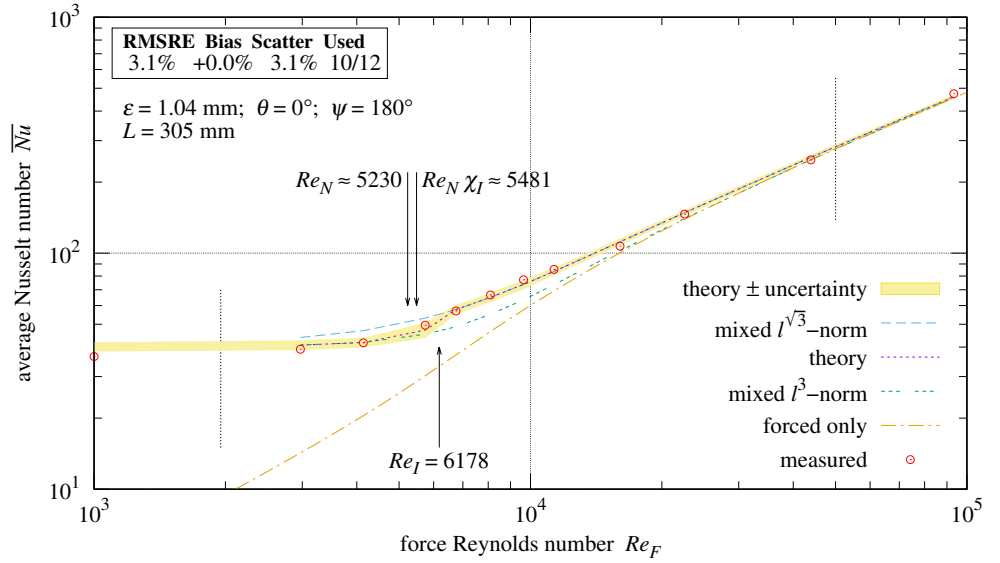


Figure 15. Vertical plate in opposing forced turbulent flow.

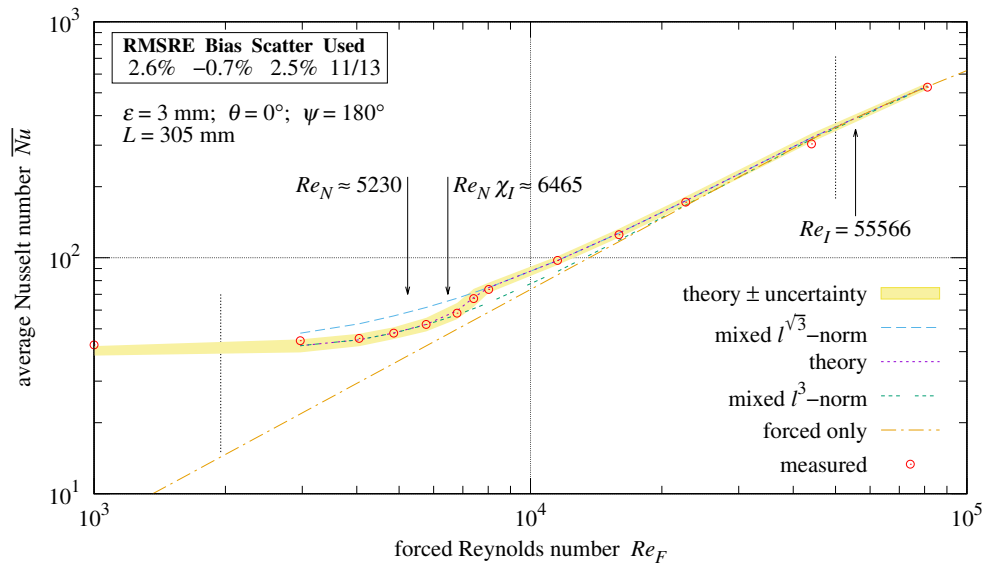


Figure 16. Vertical plate in opposing forced rough flow.

6.3. Vertical plate with forced upward flow

At low speeds, the wide separation between the “forced + natural 5400” and “forced 5400” traces in Figure 14 indicates the boundary layer is split, with laminar natural flow near the plate and forced turbulent flow away, leading to $\bar{h} = \|\bar{h}_F, \bar{h}'\|_{\sqrt{3}}$.

The steep slope of the “forced + natural 21,600” and “forced 21,600” traces near the plate indicates that both flows are close to the plate, competing for plate area and leading to $\bar{h} = \|\bar{h}_F, \bar{h}'\|_3$.

Figures 17 and 18 show the theory curve and the measurements switching from the “mixed ℓ^3 -norm” to the “mixed $\ell^{\sqrt{3}}$ -norm” at Re_F smaller than $Re_N \chi_I$.

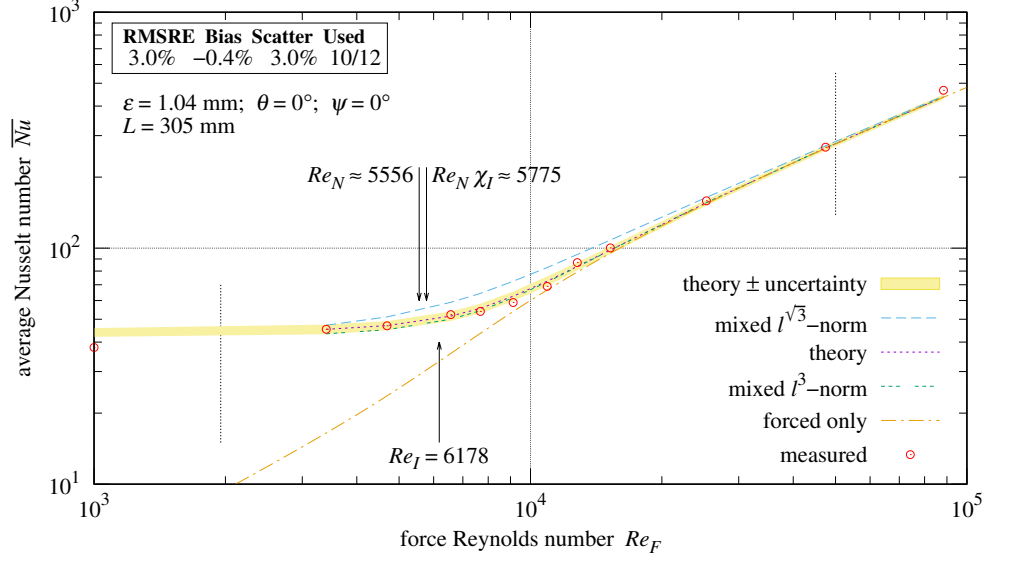


Figure 17. Vertical plate in aiding forced turbulent flow.

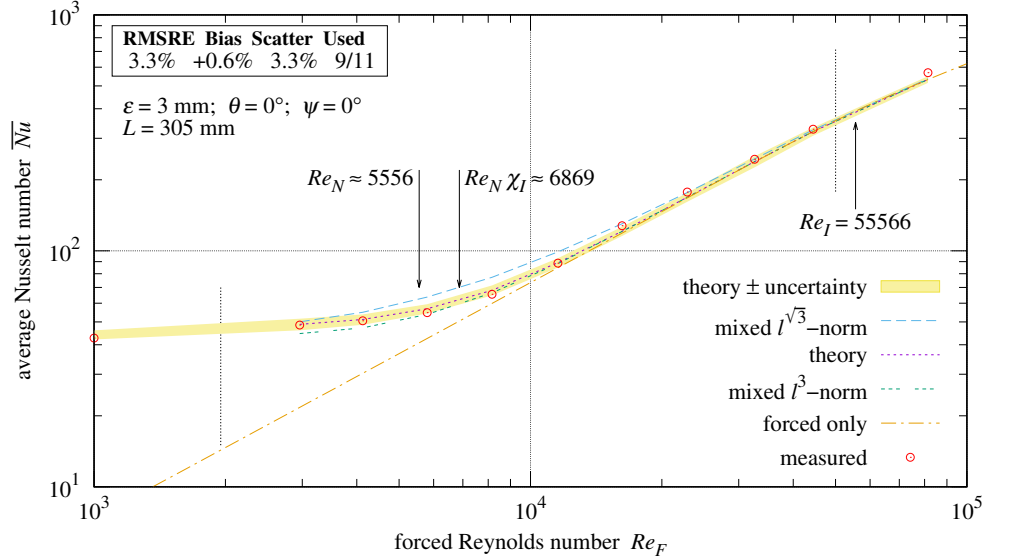


Figure 18. Vertical plate in aiding forced rough flow.

7. Vertical plate with forced flows at any angle

All vertical cases examined so far combine $\overline{h'}$ and $\overline{h_F}$ using the l^p -norm with $\sqrt{3} \leq p \leq 3$. However, p is a function of Re_F in the vertical aiding and opposing cases. Needed is a function of Re_F which varies smoothly between asymptotes $\sqrt{3}$ and 3. This suggests raising 3 to an exponent between 1/2 and 1. With $\zeta > 1$ and $\eta > 0$, the expression η^ζ/ζ varies between 0 and ∞ , and $\exp_\zeta(-\eta^\zeta/\zeta)$ varies between 0 and 1. Equation (27) varies between $p = 3$ and $p = \sqrt{3}$, with the transition slope controlled by ζ .

The aiding flow transition is gradual with $\zeta = 2$ and $\eta = Re_N \chi_I / Re_F$. The opposing flow transition is abrupt with $\zeta = 16$ and $\eta = Re_F / [Re_N \chi_I]$. Note that $\eta = Re_N \chi_I / Re_F$ differs from $\eta = Re_F / [Re_N \chi_I]$.

$$p(\zeta, \eta) = \exp_3 \left(1/2 + \exp_\zeta \left(-\eta^\zeta / \zeta \right) / 2 \right) \quad (27)$$

Introduced in Section 4, ψ is the angle between the forced flow and the zenith. **Figure 19a,b** plot p at $\zeta = 2$ and $\zeta = 16$, used with $\cos \psi > 0$ and $\cos \psi < 0$, respectively.

Table 4 lists p for horizontal and vertical plate and flows.

The theory curve and error statistics in **Figures 15–18** employ p Equation (27).

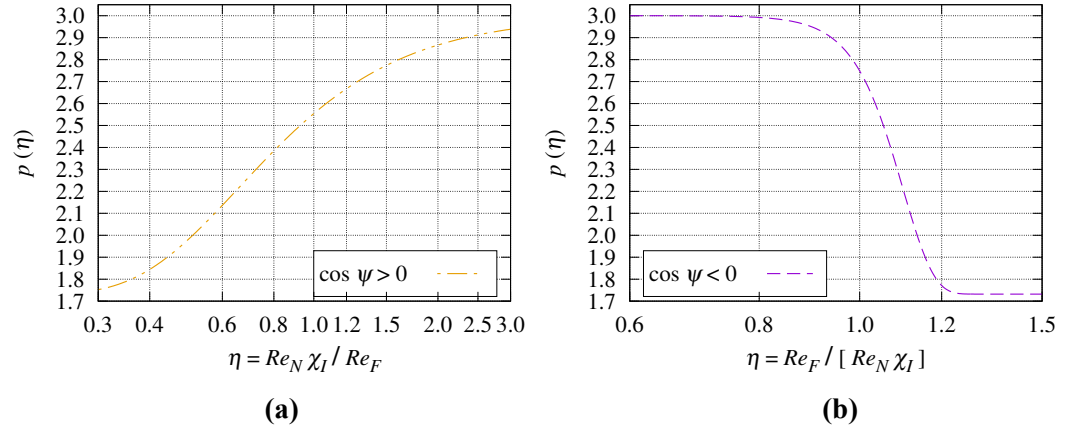


Figure 19. (a) Vertical aiding plate p and (b) Vertical opposing plate p .

Table 4. Corner cases p .

Description	θ	ψ	p
upward facing plate	-90°	90°	2
aiding vertical plate	$+0^\circ$	0°	$\exp_3 (1/2 + \exp_2 (-[Re_N \chi_I / Re_F]^2 / 2) / 2)$
vertical plate, level flow	$+0^\circ$	90°	2
opposing vertical plate	$+0^\circ$	180°	$\exp_3 (1/2 + \exp_{16} (-[Re_F / [Re_N \chi_I]]^{16} / 16) / 2)$
downward facing plate	$+90^\circ$	90°	5

At $\psi = 0^\circ$, the forced and natural flows align. As ψ tilts toward horizontal ($\pm 90^\circ$), the forced flow can be split into components aligned and perpendicular to the natural upward flow. The coefficients of these components are trigonometric functions of ψ . Tilting to the left or right of $\psi = 0^\circ$ by equal angles must transfer the same amount of heat. Thus, the trigonometric coefficients must be “even” functions of ψ , that is, $F(\psi) = F(-\psi)$. Equation (28) coefficients $[\sin \psi]^2$, $[\cos \psi]^2$, $[\sin \psi]^4$, and $[\cos \psi]^4$ are even functions of ψ .

Downward tilted flow requires a steeper transition slope around $\psi = 180^\circ$; this is implemented using $[\sin \psi]^4$ and $[\cos \psi]^4$ as the coefficients in the second line of Equation (28).

$$\bar{h}_\theta = \begin{cases} [\sin \psi]^2 \left\| \bar{h}_F, \bar{h}'_\theta \right\|_2 + [\cos \psi]^2 \left\| \bar{h}_F, \bar{h}'_\theta \right\|_{p(2, Re_N \chi_I / Re_F)} & 0 \leq \cos \psi; \\ [\sin \psi]^4 \left\| \bar{h}_F, \bar{h}'_\theta \right\|_2 + [\cos \psi]^4 \left\| \bar{h}_F, \bar{h}'_\theta \right\|_{p(16, Re_F / [Re_N \chi_I])} & \cos \psi \leq 0 \end{cases} \quad (28)$$

The vertical natural convection component is independent of ψ :

$$\bar{h}'_\theta = \bar{h}'(|\cos \theta| Ra' / \Xi) \quad (29)$$

8. Mixed convection from an inclined plate

To compute mixed convection from an inclined plate, Equation (30) replaces conductance functions \bar{h}' , \bar{h}^* , and \bar{h}_R in Equation (11) with ℓ^p -norms mixing each function with \bar{h}_F .

$$\bar{h} = \begin{cases} \left\| \bar{h}_\theta, \left\| \bar{h}_F, \bar{h}^* (|\sin \theta| Ra^*) \right\|_2 \right\|_{16} & 0 \leq \sin \theta \\ \left\| \bar{h}_\theta, \left\| \bar{h}_F, \bar{h}_R (|\sin \theta| Ra_R / \Xi) \right\|_5 \right\|_{16} & \sin \theta \leq 0 \end{cases} \quad (30)$$

Figure 20 shows forced flow opposing natural convection at $\theta = +82^\circ$ with $\psi = 98^\circ$. **Figure 21** shows forced flow aiding natural convection at $\theta = \psi = +82^\circ$. The $\theta = \psi = +90^\circ$ curve is shown for comparison.

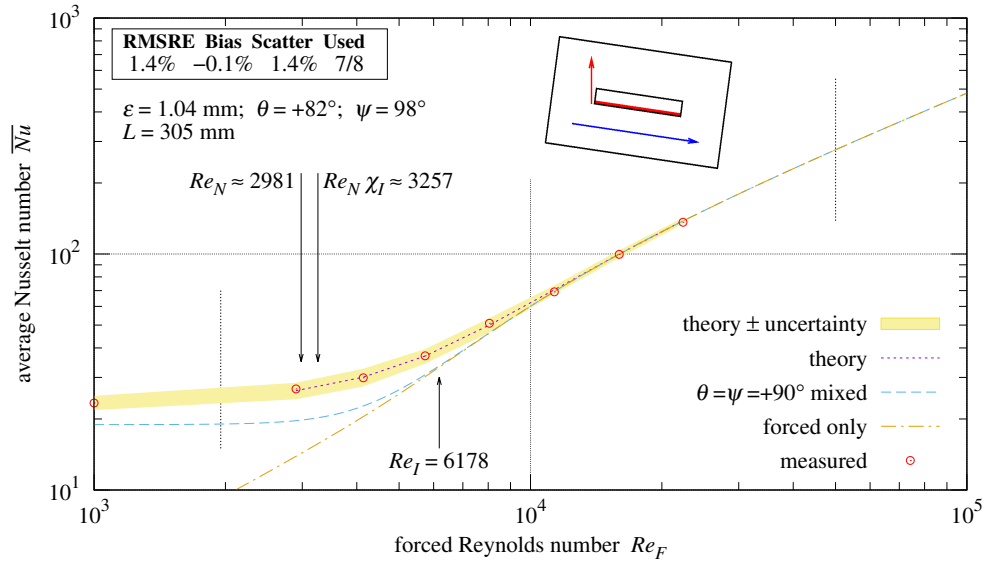


Figure 20. Inclined plate, $\theta = +82^\circ$, opposing forced turbulent flow.

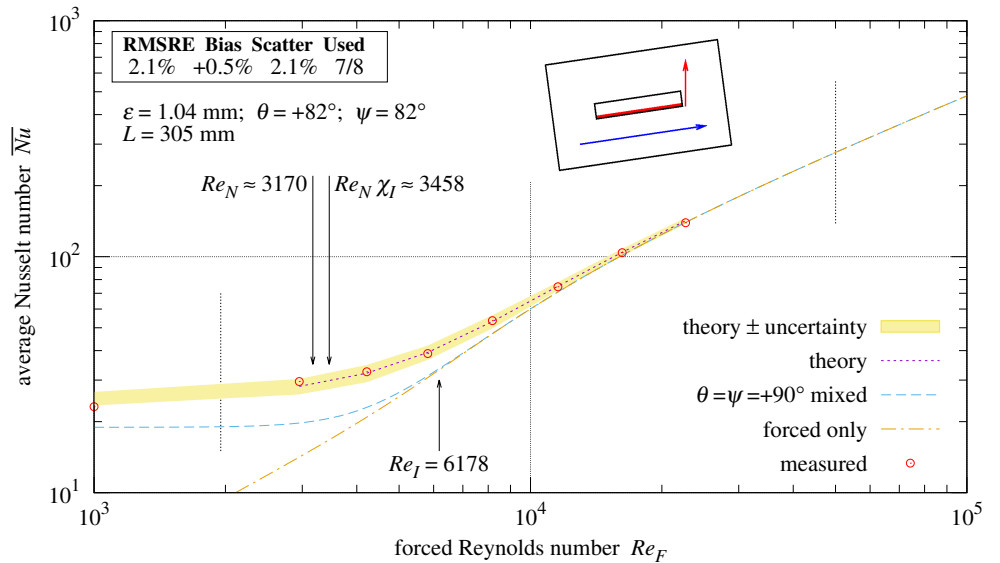


Figure 21. Inclined plate, $\theta = +82^\circ$, aiding forced turbulent flow.

With $\overline{h}_F = 0$, mixed Equation (30) simplifies to natural Equation (11).

When θ and ψ are multiples of 90° , Equation (30) simplifies to $\|\overline{h}_F, \overline{h}_N\|_p$, with p from **Table 4**.

9. Practice

The natural convection heat transfer formulas for \overline{h}^* , \overline{h}' , and \overline{h}_R were presented in Section 2. The formulas for forced convection heat transfer \overline{h}_F were presented in Section 3. These are combined using the ℓ^p -norm:

$$\|F_1, F_2\|_p \equiv [|F_1|^p + |F_2|^p]^{1/p} \quad (31)$$

θ is the angle of the plate from vertical; -90° is face up; $+90^\circ$ is face down. Coefficient $|\sin \theta|$ scales Ra^* and Ra_R to model the effect of the plate's inclination as a reduction in the gravitational acceleration.

$$\bar{h} = \begin{cases} \|\bar{h}_\theta, \|\bar{h}_F, \bar{h}^*(|\sin \theta| Ra^*)\|_2\|_{16} & 0 \leq \sin \theta \\ \|\bar{h}_\theta, \|\bar{h}_F, \bar{h}_R(|\sin \theta| Ra_R/\Xi)\|_5\|_{16} & \sin \theta \leq 0 \end{cases} \quad (32)$$

ψ is the angle of the forced flow from the zenith; $\psi = 0^\circ$ is upward flow; $\psi = 90^\circ$ is horizontal flow; $\psi = 180^\circ$ is downward flow. The forced flow is always parallel to the plate.

$$\bar{h}_\theta = \begin{cases} [\sin \psi]^2 \|\bar{h}_F, \bar{h}'_\theta\|_2 + [\cos \psi]^2 \|\bar{h}_F, \bar{h}'_\theta\|_{p(2, Re_N \chi_I / Re_F)} & 0 \leq \cos \psi; \\ [\sin \psi]^4 \|\bar{h}_F, \bar{h}'_\theta\|_2 + [\cos \psi]^4 \|\bar{h}_F, \bar{h}'_\theta\|_{p(16, Re_F / [Re_N \chi_I])} & \cos \psi \leq 0 \end{cases} \quad (33)$$

The vertical natural convection component \bar{h}'_θ is independent of ψ :

$$\bar{h}'_\theta = \bar{h}'(|\cos \theta| Ra' / \Xi) \quad (34)$$

However, its combination with \bar{h}_F depends on function $p(\zeta, \eta)$, specifically $p(2, Re_N \chi_I / Re_F)$ when $\cos \psi \geq 0$, and $p(16, Re_F / [Re_N \chi_I])$ when $\cos \psi \leq 0$:

$$p(\zeta, \eta) = \exp_3(1/2 + \exp_\zeta(-\eta^\zeta/\zeta)/2) \quad \exp_b(\varphi) \equiv b^\varphi \quad (35)$$

The χ_I factor models the longer path which forced flow takes along plateau islands roughness. The χ factor models the longer path which forced flow takes along non-plateau roughness. Re_I Equation (17) is in Section 3. Use $Re_I = +\infty$ (which implies $\chi_I = \chi$) for non-plateau roughness.

$$\chi = 1 - 3\sqrt{3} \frac{\varepsilon}{L} \ln \frac{\varepsilon}{L} \quad \chi_I = \exp_\chi\left(\exp_4\left(-[Re_F/Re_I]^4\right)\right) \quad (36)$$

Re_N is the effective Reynolds number of vertical natural convection:

$$Re_N \approx \frac{8 \bar{Nu}' \Xi^3}{Nu'_0} \quad \Xi \equiv \left\| 1, \frac{0.5}{Pr} \right\|_{\sqrt{1/3}} \quad \bar{Nu}' \equiv \frac{\bar{h}' L}{k} \quad Nu'_0 \equiv \frac{2^4}{\sqrt{2} \pi^2} \quad (37)$$

10. Results

Table 5 shows the combinations of flow types and orthogonal orientations.

Configurations measured by the present apparatus with its 0.305 m square plates are marked with \bullet .

Configurations having turbulent natural convection are marked with \circ . These would require either a larger plate and wind-tunnel or higher plate temperatures than the present apparatus supports.

Table 5. Mixed convective modes.

Natural	Forced	Vertical	Up	Down	Opposing	Aiding
laminar	turbulent	\bullet Figure 5	\bullet Figure 10	\bullet Figure 12	\bullet Figure 15	\bullet Figure 17
laminar	rough	\bullet Figure 6	\bullet Figure 11	\bullet Figure 13	\bullet Figure 16	\bullet Figure 18
turbulent	turbulent	\circ	\circ	\circ	\circ	\circ
turbulent	rough	\circ	\circ	\circ	\circ	\circ

Tables 6 and **7** summarize the present theory’s conformance with 104 measurements in twelve data-sets from the present apparatus’s two plates.

The “ ε ” column identifies the 30.5 cm square plate used. The 3.00 mm plate had rough flow over the $1950 < Re_F < 5 \times 10^4$ range. The 1.04 mm plate had turbulent flow over nearly all of the same range. The “Used” column is the count of measurements having $1950 < Re_F < 5 \times 10^4$ out of the count of measurements. Measurements at $Re_F > 5 \times 10^4$ were practically unaffected by mixing.

The $\varepsilon = 3.00$ mm data-sets have RMSRE values between 2.0% and 3.8%.

The $\varepsilon = 1.04$ mm data-sets have RMSRE values between 1.3% and 3.1%.

Table 6. Convection measurements versus present theory, forced rough flow.

Description	ε	θ	ψ	RMSRE	Bias	Scatter	Used
downward facing plate	3.00 mm	+90.0°	90.0°	3.8%	+1.0%	3.7%	10/14
upward facing plate	3.00 mm	−90.0°	90.0°	3.6%	−0.2%	3.6%	6/10
vertical plate, level flow	3.00 mm	+0.0°	90.0°	2.0%	+0.8%	1.8%	6/8
opposing vertical plate	3.00 mm	+0.0°	180.0°	2.6%	−0.7%	2.5%	11/13
aiding vertical plate	3.00 mm	+0.0°	0.0°	3.3%	+0.6%	3.3%	9/11

Table 7. Convection measurements versus present theory, forced turbulent flow.

Description	ε	θ	ψ	RMSRE	Bias	Scatter	Used
downward facing plate	1.04 mm	+90.0°	90.0°	2.6%	−0.6%	2.6%	12/15
upward facing plate	1.04 mm	−90.0°	90.0°	2.5%	+0.2%	2.4%	6/8
vertical plate, level flow	1.04 mm	+0.0°	90.0°	3.0%	+0.8%	2.8%	10/14
opposing vertical plate	1.04 mm	+0.0°	180.0°	3.1%	+0.0%	3.1%	10/12
aiding vertical plate	1.04 mm	+0.0°	0.0°	3.0%	−0.4%	3.0%	10/12
opposing inclined plate	1.04 mm	+82.0°	98.0°	1.4%	−0.1%	1.4%	7/8
aiding inclined plate	1.04 mm	+82.0°	82.0°	2.1%	+0.5%	2.1%	7/8

Table 8 summarizes the present theory’s conformance with 78 measurements in 28 data-sets on five vertical rough surfaces in horizontal flow from Rowley et al. [14]. The five stucco data-sets have RMSRE values between 2.5% and 6.5%; the other data-sets have RMSRE values between 0.2% and 5%.

11. Discussion

Developing this theory was difficult due to the lack of photographs of mixed convection streamlines along rough surfaces. Analysis of the measurements made clear that mixed convection from rough plates was different from that of smooth plates. The flow patterns had to be inferred from these measurements and knowledge of natural and forced convections.

Many theories were tried and discarded concerning the forced vertical flow cases. Examination of hypothetical velocity profiles sparked the present theory, which explains the aiding and opposing flow cases both having $\ell^{\sqrt{3}}$ -norm and ℓ^3 -norm asymptotes.

11.1. Heat transfer bounds

All of the ℓ^p -norms combining natural and forced heat transfer have $\sqrt{3} \leq p \leq 5$. The mixed heat transfer is thus bounded between $\|\overline{h_F}, \overline{h_N}\|_5$ and $\|\overline{h_F}, \overline{h_N}\|_{\sqrt{3}}$.

Table 8. Rowley et al. mixed convection measurements.

Surface	ϵ	ε	V	RMSRE	Bias	Scatter	Count
smooth-plaster	0.910	0.200 mm	15.65 m/s	3.3%	-0.8%	3.3%	2
smooth-plaster	0.910	0.200 mm	13.41 m/s	2.7%	-0.1%	2.7%	2
smooth-plaster	0.910	0.200 mm	11.18 m/s	0.6%	+0.6%	0.1%	2
smooth-plaster	0.910	0.200 mm	8.94 m/s	1.5%	+1.5%	0.3%	2
smooth-plaster	0.910	0.200 mm	6.71 m/s	2.4%	+2.3%	0.8%	2
smooth-plaster	0.910	0.200 mm	4.47 m/s	2.7%	+1.3%	2.4%	2
concrete	0.940	0.550 mm	15.65 m/s	0.2%	-0.2%	0.0%	1
concrete	0.940	0.550 mm	13.41 m/s	2.3%	-0.1%	2.3%	3
concrete	0.940	0.550 mm	11.18 m/s	2.5%	-1.0%	2.3%	7
concrete	0.940	0.550 mm	8.94 m/s	4.7%	-3.6%	3.0%	2
concrete	0.940	0.550 mm	6.71 m/s	2.4%	+0.1%	2.4%	2
concrete	0.940	0.550 mm	4.47 m/s	4.1%	+4.1%	0.3%	2
brick	0.930	0.750 mm	12.67 m/s	4.7%	-3.8%	2.8%	6
brick	0.930	0.750 mm	10.95 m/s	3.6%	+0.0%	3.6%	4
brick	0.930	0.750 mm	8.94 m/s	4.4%	-1.6%	4.1%	3
brick	0.930	0.750 mm	8.00 m/s	2.5%	+1.4%	2.1%	5
brick	0.930	0.750 mm	5.99 m/s	4.4%	+4.3%	0.8%	4
brick	0.930	0.750 mm	3.38 m/s	2.9%	-0.2%	2.9%	4
rough-plaster	0.910	0.750 mm	13.41 m/s	2.6%	-2.6%	0.0%	1
rough-plaster	0.910	0.750 mm	11.18 m/s	2.5%	-2.0%	1.5%	2
rough-plaster	0.910	0.750 mm	8.94 m/s	1.3%	+0.8%	1.1%	2
rough-plaster	0.910	0.750 mm	6.71 m/s	0.5%	-0.1%	0.4%	3
rough-plaster	0.910	0.750 mm	4.47 m/s	1.7%	-0.9%	1.5%	2
stucco	0.910	1.500 mm	13.41 m/s	6.8%	-6.7%	1.0%	2
stucco	0.910	1.500 mm	11.18 m/s	3.3%	-2.9%	1.6%	3
stucco	0.910	1.500 mm	8.94 m/s	2.1%	+1.5%	1.4%	3
stucco	0.910	1.500 mm	6.71 m/s	5.4%	+4.9%	2.3%	3
stucco	0.910	1.500 mm	4.47 m/s	5.7%	+5.7%	0.6%	2

11.2. Horizontal flow obstruction

The fan pulling air through the chamber is sufficient to counter the effect of the wind-tunnel's obstructions to horizontal flow, except in the case of the vertical plate with opposing flow. In order to draw some air upward at slow (downward) fan speeds, the air's momentum must be reversed. This is modeled by increasing parameter B of **Table 2** by twice the vertical distance from the plate to the test chamber upper edge, normalized by L and the ratio of the upper edge perimeter to the plate width. This same correction applies to still air in the vertical tunnel.

11.3. Effective vertical Reynolds number

Aiding and opposing vertical plate measurements in a fluid other than air are needed to further test the effective vertical Reynolds number, Re_N Equation (9).

11.4. Rough velocity profiles

The hypothetical forced flows in the Section 6 velocity profiles were turbulent flows. Measurements of both vertical plates in vertical flow conforming to the present theory suggests that the rough and turbulent velocity profiles are similar.

11.5. Duct velocity profile

The aggregate boiling point kinematic viscosity $\bar{\nu}_0$ in Equation (22) may be useful in developing formulas for pipe and duct velocity profiles as a function of duct length.

12. Conclusions

Formulas were presented for predicting the mixed convective surface conductance of a flat isotropic surface roughness having a convex perimeter in a Newtonian fluid with a steady forced flow in the plane of that roughness.

The prerequisites are the RMS height-of-roughness $0 < \varepsilon$, angle θ of the surface from vertical, angle ψ of the forced flow from the zenith, Ra/L^3 and Pr of the fluid, and the characteristic-length $L > 0$ and $Re > 0$ of the forced flow.

- RMS height-of-roughness ε is the correct metric for predicting forced convective surface conductance.
- Roughness $\varepsilon \ll L$ does not affect the natural component of mixed convection.
- Plate inclination does not affect the forced component of mixed convection.
- When $Re = 0$, the mixed convection is the same as its natural component.

The present work's formulas were compared with 104 measurements in twelve data-sets from the present apparatus in two inclined and all five corner case orientations. The twelve data-sets had RMSRE values between 1.3% and 4% relative to the present theory.

The present work's formulas were compared with 78 measurements in 28 data-sets on five vertical rough surfaces in horizontal airflow from Rowley et al. [14]. The five stucco data-sets had RMSRE values between 2.5% and 6.5%; the other data-sets had RMSRE values between 0.2% and 5%.

Supplementary materials: A zip archive of PDF files of graphs and estimated measurement uncertainties of each 102-min time-series producing a convection measurement can be downloaded from: <http://people.csail.mit.edu/jaffer/convect>. A zip archive of the aggregate measurements is also available from the site.

Author contributions: Conceptualization, AJ and MJ; methodology, AJ; software, AJ; validation, AJ; formal analysis, AJ; investigation, AJ and MJ; resources, AJ; data curation, AJ; writing—original draft preparation, AJ; writing—review and editing, MJ; visualization, MJ and AJ; supervision, AJ; project administration, AJ; funding acquisition, AJ. All authors have read and agreed to the published version of the manuscript.

Acknowledgments: Thanks to John Cox (1957–2022) and Doug Ruuska for machining the bi-level plate. Thanks to Roberta Jaffer for assistance and problem-solving suggestions. Thanks to anonymous reviewers for their useful suggestions.

Conflict of interest: The authors declare no conflict of interest.

Nomenclature

Latin letters

A	surface area (m^2)
Gr	Grashof number
\bar{h}	average convective surface conductance ($\text{W}/(\text{m}^2 \cdot \text{K})$)
\bar{h}_F	forced convective surface conductance ($\text{W}/(\text{m}^2 \cdot \text{K})$)
\bar{h}_N	natural convective surface conductance ($\text{W}/(\text{m}^2 \cdot \text{K})$)
\bar{h}^*	upward natural convective surface conductance ($\text{W}/(\text{m}^2 \cdot \text{K})$)
\bar{h}'	vertical plate natural convective surface conductance ($\text{W}/(\text{m}^2 \cdot \text{K})$)
\bar{h}_θ	vertical mode of inclined natural convective surface conductance ($\text{W}/(\text{m}^2 \cdot \text{K})$)
\bar{h}'_θ	vertical component of \bar{h}_θ ($\text{W}/(\text{m}^2 \cdot \text{K})$)
\bar{h}_R	downward natural convective surface conductance ($\text{W}/(\text{m}^2 \cdot \text{K})$)
k	fluid thermal conductivity ($\text{W}/(\text{m} \cdot \text{K})$)
L	characteristic length (m)
L_P	roughness spatial period (m)
L^*	ratio of plate area to its perimeter (m)
L^\bullet	ratio of island area to its perimeter (m)
L_W	width of plate (m)
\bar{Nu}	average Nusselt number
\bar{Nu}_N	average Nusselt number of natural convection
\bar{Nu}'	average Nusselt number of vertical plate natural convection
Nu'_0	Nusselt number of vertical plate conduction
p	exponent in ℓ^p -norm: $\{ F_1 ^p + F_2 ^p\}^{1/p}$
Pr	Prandtl number of the fluid
Ra	Rayleigh number
Ra'	vertical plate Rayleigh number
Ra^*	upward Rayleigh number
Ra_R	downward Rayleigh number
Re_F	Reynolds number of the forced flow parallel to the plate
Re_I	Reynolds number of rough turbulent transition to forced turbulent flow
Re_N	effective Reynolds number of vertical natural convection
Re_y	friction Reynolds number
$u(y)$	velocity at $x = L/2$ and distance y from the plate (m/s)
u_N	effective natural flow speed = $\nu Re_N/L$ (m/s)
u^*	friction velocity (m/s)
W_0	principal branch of the Lambert W function
y	distance from plate (m)
\bar{z}	average roughness elevation (m)

Greek symbols

δ	boundary layer thickness (m)
δ_λ	laminar boundary layer thickness (m)
δ_τ	turbulent boundary layer thickness (m)
ϵ	surface emissivity
ε	surface RMS height-of-roughness (m)
η	ratio of Re_N and Re_F (either order)
κ	von Kármán constant ≈ 0.41
Ω	ratio of non-plateau area to cell area (m^2/m^2)
ν	fluid kinematic viscosity (m^2/s)
ν_0	gas kinematic viscosity (m^2/s) at boiling point
ψ	angle between the forced flow and the zenith; 0° is aiding flow; 180° is opposing flow
θ	angle of the plate surface from vertical; face up is -90° ; face down is $+90^\circ$
Ξ	natural convection self-obstruction factor
χ	roughness velocity correction factor for forced flow
χ_I	plateau islands roughness correction factor

Notes

- ¹ Schlichting [19] describes a boundary-layer: “In that thin layer the velocity of the fluid increases from zero at the wall (no slip) to its full value which corresponds to external frictionless flow.”
- ² One outlying measurement for brick at $V = 15.65$ m/s was omitted.

References

- Lienhard JH. Heat Transfer in Flat-Plate Boundary Layers: A Correlation for Laminar, Transitional, and Turbulent Flow. *Journal of Heat Transfer*. 2020; 142(6): 04.
- Jaffer A. Skin-friction and forced convection from rough and smooth plates. *Thermo*. 2023; 3(4): 711–775. doi: 10.3390/thermo3040040
- Fujii T, Imura H. Natural-convection heat transfer from a plate with arbitrary inclination. *International Journal of Heat and Mass Transfer*. 1972; 15(4): 755–764. doi: 10.1016/0017-9310(72)90118-4
- Churchill SW, Chu HHS. Correlating equations for laminar and turbulent free convection from a vertical plate. *International Journal of Heat and Mass Transfer*. 1975; 18(11): 1323–1329. doi: 10.1016/0017-9310(75)90243-4.
- Jaffer A. Natural convection heat transfer from an isothermal plate. *Thermo*. 2023; 3(1): 148–175. doi: 10.3390/thermo3010010
- Churchill SW, Usagi R. A general expression for the correlation of rates of transfer and other phenomena. *AIChE Journal*. 1972; 18(6): 1121–1128. doi:10.1002/aic.690180606
- Hieber CA. Mixed convection above a heated horizontal surface. *International Journal of Heat and Mass Transfer*. 1973; 16(4): 769–785. doi: 10.1016/0017-9310(73)90090-2
- Wang XA. An experimental study of mixed, forced, and free convection heat transfer from a horizontal flat plate to air. *Journal of Heat Transfer*. 1982; 104(1): 139–144. doi: 10.1115/1.3245040
- Siebers DL, Schwind RG, Moffat RJ. Experimental mixed-convection heat transfer from a large, vertical surface in a horizontal flow. Technical report, Sandia National Lab; 1983.
- Ramachandran N, Armaly BF, Chen TS. Measurements and Predictions of Laminar Mixed Convection Flow Adjacent to a Vertical Surface. *Journal of Heat Transfer*. 1985; 107(3): 636–641. doi: 10.1115/1.3247471
- Lin HT, Yu WS, Chen CC. Comprehensive correlations for laminar mixed convection on vertical and horizontal flat plates. *Wärme-und Stoffübertragung*. 1990; 25(6): 353–359.
- Kobus CJ, Wedekind JL. An experimental investigation into forced, natural and combined forced and natural convective heat transfer from stationary isothermal circular disks. *International Journal of Heat and Mass Transfer*. 1995; 38(18): 3329–3339. doi: 10.1016/0017-9310(95)00096-R

13. Kobus CJ, Wedekind JL. An experimental investigation into natural convection heat transfer from horizontal isothermal circular disks. *International Journal of Heat and Mass Transfer*. 2001; 44(17): 3381–3384. doi: 10.1016/S0017-9310(00)00330-6
14. Rowley FB, Algren AB, Blackshaw JL. Surface conductances as affected by air velocity, temperature and character of surface. *ASHVE Trans*. 1930; 36: 429–446.
15. Incropera FP, DeWitt DP, Bergman TL, Lavine AS. *Fundamentals of Heat and Mass Transfer*. Wiley; 2007.
16. Aihara T, Yamada Y, Endö S. Free convection along the downward-facing surface of a heated horizontal plate. *International Journal of Heat and Mass Transfer*. 1972;15(12): 2535–2549. doi: 10.1016/0017-9310(72)90145-7
17. Žukauskas A, Šlančiauskas A. *Heat Transfer in Turbulent Fluid Flows*. Hemisphere Publishing Corp; 1987.
18. Lienhard IV JH, Lienhard VA JH. *Heat Transfer Textbook*. Phlogiston Press; 2020.
19. Schlichting H. *Boundary-Layer Theory*. McGraw Hill; 2014.
20. Rice RW. Emittance factors for infrared thermometers used for wood products. *Wood and Fiber Science*. 2004; 36: 520–526.
21. Barreira E, Almeida RMSF, Simões ML. Emissivity of building materials for infrared measurements. *Sensors*. 2021; 21(6). doi: 10.3390/s21061961
22. Abernethy RB, Benedict RP, Dowdell RB. Asme measurement uncertainty. *ASME. J. Fluids Eng*. 1985; 107(2): 161–164. doi: 10.1115/1.3242450

Appendix A

I. Velocity profiles

This investigation assumes that the laminar natural boundary layer thickness δ_λ is the same as the forced laminar thickness calculated using the effective vertical Re_N . Formulas from Lienhard and Lienhard [18] lead to natural convection velocity profile $u(y)$ Equation (A1), where y is the horizontal distance from the mid-line of the vertical plate, ν is the fluid's kinematic viscosity, and $u_N = \nu Re_N/L$ is the effective natural flow speed.

$$u(y) \approx 4 u_N \frac{y}{\delta_\lambda} \left[1 - \frac{y}{\delta_\lambda} \right]^2 \quad 0 < y < \delta_\lambda \approx \frac{4.92 L}{\sqrt{Re_N}} \quad (A1)$$

In forced turbulent flow along a smooth plate, let friction velocity $u^* \approx u_\infty \sqrt{f_\tau/2}$, and $Re_y = u^* y/\nu$, with \bar{f}_τ from Equation (15). Lienhard and Lienhard [18] gives the viscous sublayer velocity profile as Equation (A2), and the log-layer velocity profile as Equation (A3). The von Kármán constant $\kappa \approx 0.41$.

$$\frac{u(y)}{u^*} \approx Re_y \quad Re_y < 7 \quad (A2)$$

$$\frac{u(y)}{u^*} \approx \left[\frac{1}{\kappa} \ln(Re_y) + 5.5 \right] \quad Re_y > 30 \quad (A3)$$

Lienhard and Lienhard [18] does not tell how to interpolate these two formulas. The $7 < Re_y < 30$ range to be interpolated is large, and the transition must be gradual. Adapting the staged-transition formula from Jaffer [2] by using the $\ell^{-\sqrt{1/3}}$ -norm instead of the ℓ^{-4} -norm in Re_Y Equation (A4) yields Equation (A5).

$$Re_Y = \|7, Re_y\|_{-\sqrt{1/3}} \quad y < \delta_\tau \approx \frac{0.37 L}{\sqrt[5]{Re}} \quad (A4)$$

$$\frac{u(y)}{u^*} = \left[5.5 + \frac{\ln(Re_y)}{\kappa} \right] + \frac{Re_Y}{Re_y} \left[Re_Y - 5.5 - \frac{\ln(Re_Y)}{\kappa} \right] \quad (A5)$$

Equation (A6) is a proposed alternative to Equation (A5) based on the Lambert W_0 function.

$$\frac{u(y)}{u^*} = \frac{8}{\sqrt{3}} W_0(\sqrt{3} Re_y) \quad (A6)$$

The “interpolated” Equation (A5) and Equation (A6) curves are nearly identical in **Figure A1**. It is not surprising that a formula for turbulent flow involves the Lambert W_0 function. Equation (A6) uses $W_0(\sqrt{3} Re_y)$ while \bar{f}_τ Equation (15) uses $W_0(Re_F/\sqrt{3})$.

While interesting, these curves are employed only for estimating the net vertical flow near the plate. None of the convective surface conductance formulas quantitatively depend on them.

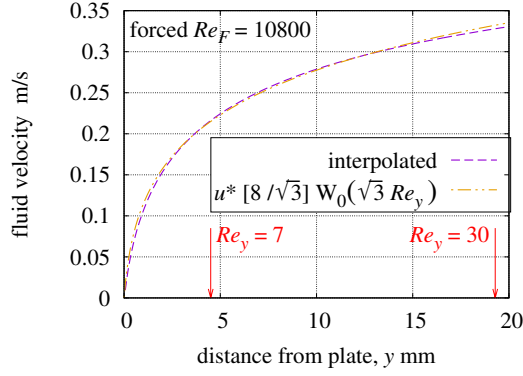


Figure A1. Forced convection velocity profile.

II. Rough plates

Because roughness $\varepsilon \ll L$ has negligible effect on natural convection, u_N should be the same from smooth and rough plates. Hence, their $Re_N \equiv u_N \varepsilon / \nu$ should also be equal.

Forced flow along a rough surface traverses a path longer than L . The effective Re_N/Re_F ratio of a rough surface should be increased by a function of the “roughness Reynolds number” Re_ε Equation (A7).

$$Re_\varepsilon = \frac{u^* \varepsilon}{\nu} = \frac{Re}{\sqrt{3} [L/\varepsilon] \ln(L/\varepsilon)} \quad (\text{A7})$$

Proposed is Re_N/Re scale factor χ Equation (A8), where Re is the solution of Equation (A7) combined with $Re_\varepsilon = 3 [\varepsilon/L]^2$. **Figure A2a** graphs χ as a function of ε .

$$\chi = \frac{Re_F + Re}{Re_F} = 1 - 3\sqrt{3} \frac{\varepsilon}{L} \ln \frac{\varepsilon}{L} \quad (\text{A8})$$

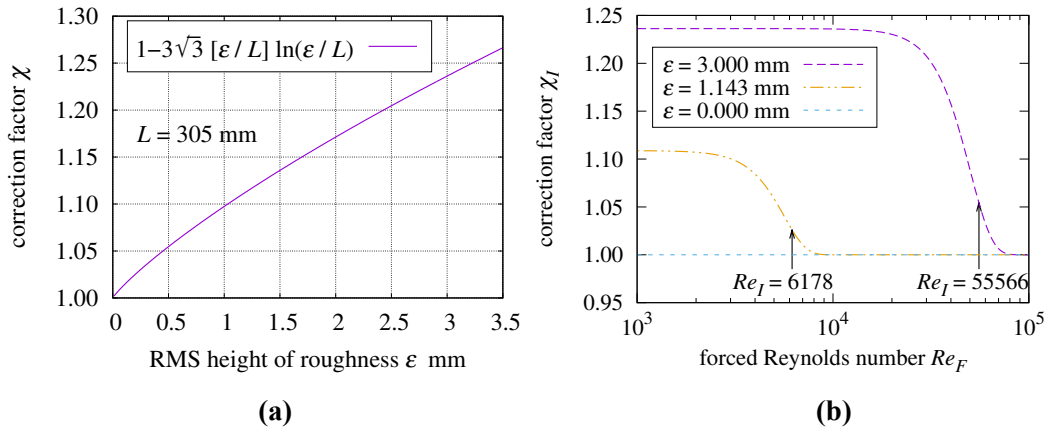


Figure A2. (a) χ versus ε and (b) Re_N correction factor χ_I .

Appendix B

Plateau islands roughness correction

Plates shedding only turbulent flow have $\chi_I = 1$. Plates shedding only rough flow have $\chi_I = \chi$ from Equation (A8).

Plateau roughness (forced) convection transitions from rough flow to turbulent flow as the ℓ^{-4} -norm in Equation (18). The scale factor χ_I should vary between 1 and χ as a function of Re_F . Expression $\exp_4(-[Re_F/Re_I]^4)$ varies between 0 and 1. Proposed is χ_I , the Re_N/Re_F scale factor:

$$\chi_I = \exp_{\chi}(\exp_4(-[Re_F/Re_I]^4)) \quad (\text{B1})$$

Note the similarity of Equation (B1) and Equation (27) with $\zeta = 4$.

Figure A2b plots χ_I with $\varepsilon = 3$ mm, $\varepsilon = 1.143$ mm, and $\varepsilon = 0$.

Appendix C

I. Apparatus and measurement methodology

The original goal of the present apparatus was to measure forced convection heat transfer from a precisely rough plate over the widest practical span of airflow velocities. To minimize natural convection, it measured downward natural convection mixed with horizontal forced flow. Its measurements are presented in Jaffer [2].

Although more complicated to analyze, the plate was suspended, not embedded, in the wind-tunnel. The measurements from prior investigations which embedded the plate in a wind-tunnel wall were largely incompatible with the present theory because their flows were not isobaric.

The small size of the wind-tunnel chassis (1.3 m × 0.61 m × 0.65 m) afforded an opportunity to characterize mixed convection at other orientations of the plate and flow.

II. The plate

Figure C1a shows the rough surface of the test plate; it was milled from a slab of MIC-6 aluminum (Al) to have (676 of) square 8.33 mm × 8.33 mm × 6 mm posts spaced on 11.7 mm centers over the 30.5 cm × 30.5 cm plate. The area of the top of each post was 0.694 cm², which was 50.4% of its 1.38 cm² cell. The RMS height-of-roughness $\varepsilon = 3.00$ mm. Openness $\Omega \approx 49.6\%$. Embedded in the plate are 9 electronic resistors as heating elements and a Texas Instruments LM35 Precision Centigrade Temperature Sensor. 2.54 cm of thermal insulating foam separates the back of the plate from a 0.32 mm thick sheet of aluminum with an LM35 at its center. **Figure C1b** is a cross-section illustration of the plate assembly.

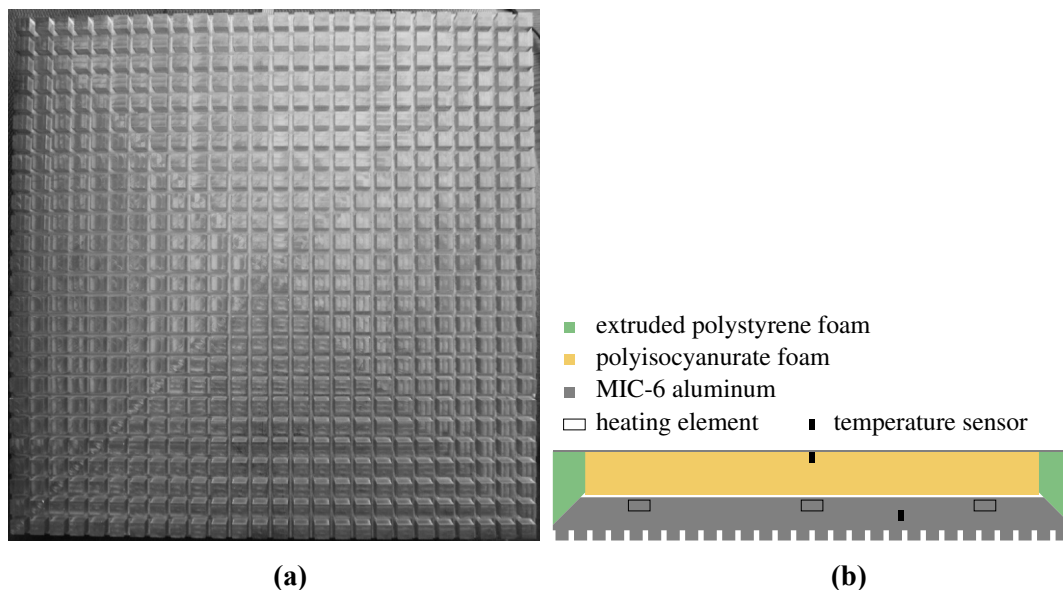


Figure C1. (a) Rough surface of plate and (b) Plate assembly cross-section.

III. Wind tunnel

The fan pulls air from the test chamber's open intake through the test chamber. The fan blows directly into a diffuser made of folded plastic mesh to disrupt vortices generated by the fan. In a sufficiently large room, the disrupted vortices dissipate before being drawn into the open intake.

To guarantee isobaric (no pressure drop) flow, the wind-tunnel must be sufficiently large that its test chamber and plate assembly boundary-layers do not interact at fan-capable airspeeds.

The wind-tunnel test chamber in **Figure C2a** has a 61 cm × 35.6 cm cross-section and a 61 cm depth. This allows the plate assembly to be centered in the wind-tunnel with 15 cm of space on all sides. The fan pulling air through the test chamber produces a maximum airspeed of 4.65 m/s ($Re \approx 9.2 \times 10^4$ along the 30.5 cm square plate). Its minimum nonzero airspeed is 0.12 m/s ($Re \approx 2300$).

Test chamber laminar and turbulent 99% boundary-layer thicknesses ([19]) are:

$$\delta_\lambda = 4.92 \sqrt{\frac{x\nu}{u}} \quad \delta_\tau = 0.37 x^{4/5} \left[\frac{\nu}{u} \right]^{1/5} \quad (C1)$$

Figure C2b shows that the 15 cm clearance between the plate and the test chamber walls is sufficient to prevent their boundary-layers from interacting at airspeeds within the fan’s capabilities.

The plate assembly (face down in **Figures C1b** and **C2a**) is suspended by six lengths of 0.38 mm-diameter steel piano wire terminated at twelve zither tuning pins in wooden blocks fastened to the exterior of the test chamber. With the plate assembly in the test chamber, the airspeed increases in proportion to the reduction of test chamber aperture A_e by the plate’s cross-sectional area A_x :

$$\frac{u_x}{u} = \frac{A_e}{A_e - A_x} \approx 107.6\% \quad (C2)$$

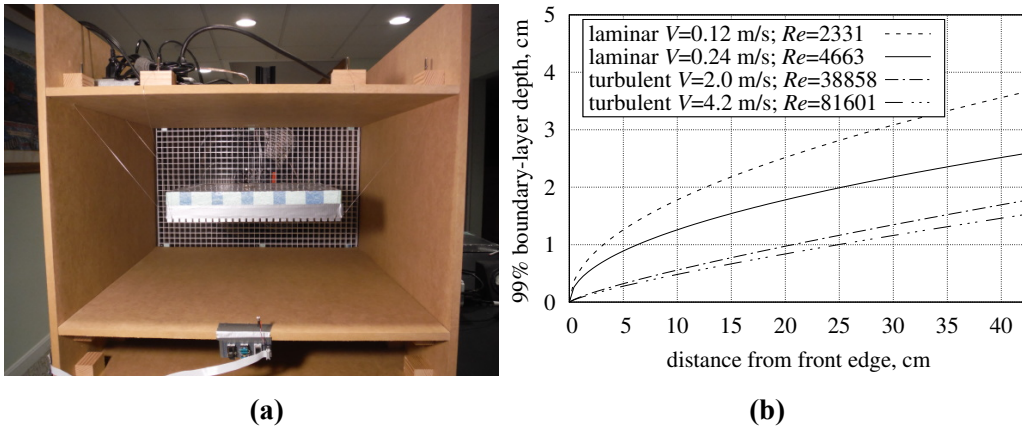


Figure C2. (a) $\varepsilon = 3$ mm plate in wind-tunnel and (b) Wind-tunnel boundary-layers.

IV. Automation

Data capture and control of convection experiments are performed by an “STM32F3 Discovery 32-Bit ARM M4 72MHz” development board. The program written for the STM32F3 captures readings and writes them to the microprocessor’s non-volatile RAM, controls the plate heating, servos the fan speed, and later uploads its data to a computer through a USB cable.

Once per second during an experiment, the program calibrates and reads each on-chip 12 bit analog-to-digital converter 16 times, summing the sixteen 12 bit readings to create a 16 bit reading per converter.

Rotations of the fan are sensed when a fan blade interrupts an infrared beam. The microprocessor controls a solid-state relay (supplying power to the fan) to maintain a fan rotation rate, ω , which is dialed into switches. At $\omega \leq 210$ r/min, the microprocessor pulses power to the fan to phase-lock the beam interruption signal to an internal clock. At $\omega > 210$ r/min, the microprocessor servos the duty cycle of a 7.5 Hz square-wave gating power to the fan. This system operates at $32 \text{ r/min} < \omega < 1400 \text{ r/min}$.

V. Calibration

The correspondence between fan rotation rate ω and test chamber airspeed u was determined using an “Ambient Weather WM-2”, which specifies an accuracy of $\pm 3\%$ of reading. After 2017 an “ABM-200 Airflow & Environmental Meter” specifying an accuracy of $\pm 0.5\%$ of reading between 2.2 m/s and 62.5 m/s, was used.

The “UtiliTech 20 inch 3-Speed High Velocity Floor Fan” has three blades with maximum radius $r = 0.254$ m. Its characteristic length is its hydraulic-diameter, $D_H = 0.550$ m. The velocity of the blade tips is $2\pi r \omega / 60$, where ω is the number of rotations per minute. The Reynolds number of the fan is:

$$Re_f = \frac{2\pi r D_H \omega / 60}{3\nu} \quad (C3)$$

The 3 blade tips trace the whole circumference in only 1/3 of a rotation, hence the 3 in the denominator.

Faster fan rotation ω yields diminishing increases of test-chamber airspeed u_t , suggesting Equation (C4), where u_u is the

limiting velocity for arbitrarily fast rotation, and coefficient η converts fan Re_f to test-chamber Re_t . **Figure C3** gives the parameters and measurements at $300 \text{ r/min} \leq \omega \leq 1500 \text{ r/min}$. The “3mm” points are the WM-2 measurements of the 3 mm plate in the original wind-tunnel; The “1mm” points are the ABM-200 measurements of the 1 mm plate in the tunnel with a new diffuser and fan cowling.

$$Re_t = \|\eta Re_f, D_H u_u/\nu\|_{-2} \quad u_t = \|\pi \eta r \omega/90, u_u\|_{-2} \tag{C4}$$

Airspeeds slower than 2 m/s should be nearly proportional to ω . Both anemometers show evidence of dry (bearing) friction in **Figure C3**. The ABM-200 “meter predictions” trace plots $1.125 u_t - 0.381$; the WM-2 “meter predictions” trace plots $1.477 u_t - 0.81$ when $u_t < 1.725$ and u_t otherwise. A mistake in the 2016 measurement software under-counted fan rotations at $\omega > 1200 \text{ r/min}$. It is compensated by replacing ω in Equations (C3, C4) with $[\omega^{-6} - 1750^{-6}]^{-1/6}$ in the WM-2 “meter predictions”. The RMSRE and Bias are relative to the “meter predictions”. The second “1mm” row includes the point at 400 r/min.

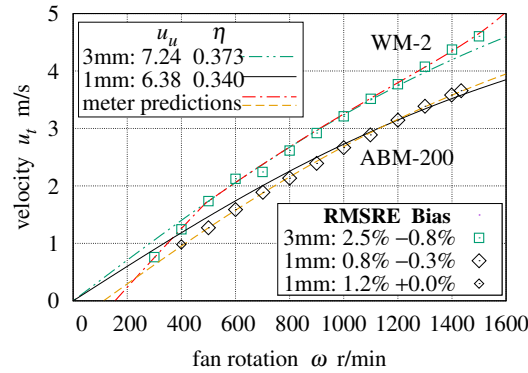


Figure C3. Airspeed versus fan speed.

Figure C4a,b show the fan speed variability in each experiment; these are used in the measurement uncertainty calculations.

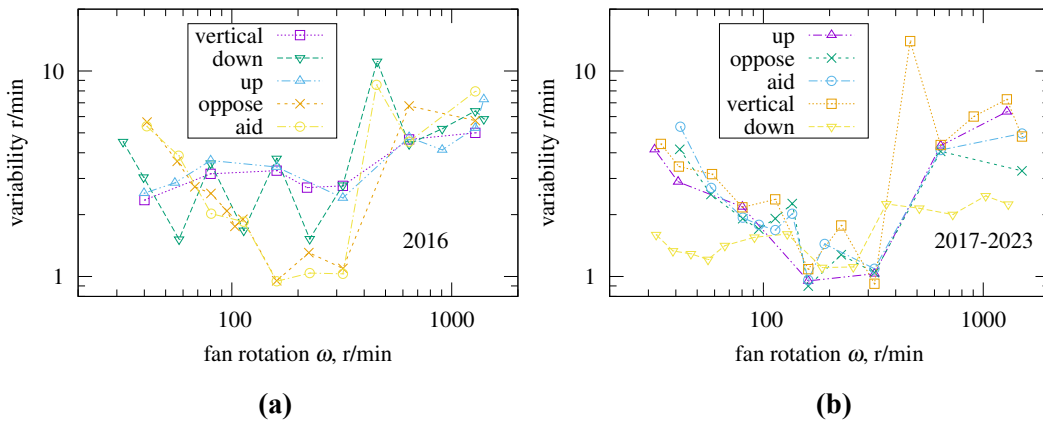


Figure C4. (a) Fan variability 3 mm plate and (b) Fan variability 1 mm plate.

VI. Ambient sensing

Figure C5a shows the ambient sensor board which was at the lower edge of the test chamber in **Figure C2a**. It measures the pressure, relative humidity, and air temperature at the wind-tunnel intake. Wrapped in aluminum tape to minimize radiative heat transfer, the LM35 temperature sensor projects into the tunnel. To minimize self-heating, the LM35 is powered only while being sampled.

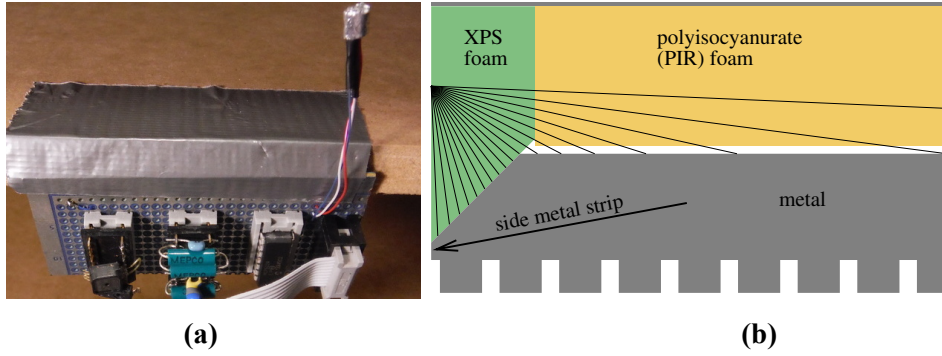


Figure C5. (a) Ambient sensors and (b) XPS wedge conduction.

VII. Physical parameters

Table C1 lists the static parameters from measurements and specifications.

The effective ϵ_{wt} may differ from the medium-density-fiberboard emissivity given by Rice [20] because the temperatures of the test chamber surfaces may not be uniform. Through the open intake, the plate also exchanges thermal radiation with objects in the room having different temperatures.

Table C1. Physical parameters.

Symbol	Values	Description
L	0.305 m	length of flow along test-surface
A	0.093 m ²	area of test-surface
ϵ	3.00 mm 1.04 mm	RMS height-of-roughness
C_{pt}	4691 J/K 4274 J/K	plate thermal capacity
D_{Al}	19.4 mm	metal slab thickness
D_{PIR}	25.4 mm	polyisocyanurate (PIR) foam thickness
D_w	19.05 mm	XPS foam wedge height
k_{PIR}	0.0222 W/(m · K)	PIR foam thermal conductivity
k_{XPS}	0.0285 W/(m · K)	XPS foam thermal conductivity
U_I	0.075 W/K	front-to-back insulation thermal conductance
ϵ_{Al}	0.04	test-surface (MIC-6 Al) emissivity
ϵ_{XPS}	0.515	XPS foam emissivity (see text)
ϵ_{dt}	0.89	duck tape emissivity
ϵ_{wt}	0.90	test chamber interior emissivity

VIII. The 1 mm roughness plate

When the 6 mm posts were milled down to 2 mm height, the four corner posts were left at their 6 mm height in order to preserve the wire suspension. This resulted in $\epsilon = 1.04$ mm for the plate as a whole. However, Re_I occurs within the first few rows of posts. $\epsilon = 1.143$ mm over the first three rows of posts results in $Re_I = 6178$.

IX. Modeling of parasitic heat flows

The plate has six surfaces from which heat can flow. At low airflow velocities, the sides of the insulation behind the test plate can leak more heat than the test-surface transfers, shrinking to 6% at 1300 r/min.

In order to measure natural convection from the (rough) test surface, natural convection and thermal radiation from the four sides (U_S) and back must be deducted from the total heat flow. Heat from the front plate flows through thermal insulating foam to a thin aluminum sheet with a temperature sensor at its center. This heat flow is simply $U_I [T_P - T_B]$, the product of the foam's thermal

conductance and the temperature difference across it.

X. Forced convection side model

The four sides are not isothermal; a 3.5 mm metal strip (see cross-section **Figure C5** runs the length of the side; and a D_w -tall wedge of extruded polystyrene foam (XPS) insulation fills the metal slab's 27 mm ($= \sqrt{2} D_{A1}$) 45° chamfer. The local surface conductance $h_W(z)$ at elevation z (from the wedge point) is found by averaging the reciprocal distance to slab metal with respect to angle θ :

$$\begin{aligned} h_W(z) &= \int_0^{\theta_c} \frac{k_{\text{XPS}}}{\sqrt{2} z \theta_c} \cos\left(\theta + \frac{\pi}{4}\right) d\theta + \int_{\theta_w}^{\theta_W} \frac{k_{\text{PIR}}}{z - D_w} \frac{\cos \theta}{\theta_W - \theta_w} d\theta \\ &= \frac{k_{\text{XPS}}}{\sqrt{2} z \theta_c} \left[\sin\left(\theta_c + \frac{\pi}{4}\right) - \sin\frac{\pi}{4} \right] + \frac{k_{\text{PIR}}}{z - D_w} \left[\frac{\sin \theta_W - \sin \theta_w}{\theta_W - \theta_w} \right] \\ \theta_c &= \arctan \frac{D_w - z}{D_w} \quad \theta_w = \arctan \frac{D_w}{z - D_w} \quad \theta_W = \max\left(\theta_w, \arctan \frac{L - D_w}{z - D_w}\right) \end{aligned} \quad (\text{C5})$$

Forced air flows parallel to the long dimension on two sides, but flows into the windward side and away from the leeward side. Air heated by the windward side reduces heat transfer from the test-surface; air heated by the test-surface suppresses heat transfer from the leeward side. Hence, the model excludes windward and leeward forced convection. The average forced convective conductance of the flow-parallel foam wedges is calculated by integrating $h_W(z)$ in series (reciprocal of the sum of reciprocals, which is also the ℓ^{-1} -norm) with the local surface conductance $k Nu_\sigma(Re_x)/L$, where $Nu_\sigma(Re_x)$ is the local pierced-laminar convection from Jaffer [2]:

$$U_W = \int_0^{D_w} \int_0^L \left\| \left\| h_W(z), \frac{k Nu_\sigma(Re_x)}{L} \right\| \right\|_{-1} dx dz \quad (\text{C6})$$

XI. Other side models

The heat flow through the four sides U_S will be estimated from the plate and ambient temperatures. While the forced convective surface conductance of the sides is modeled by integrating the local forced surface conductance, this is not generally possible for natural convection.

Natural convection formulas are known for some convex surfaces. The plate's side metal surface is not convex.

Instead, the effective side width L_{es} and effective emissivity ϵ_W are introduced into the model. The natural convection of each side is calculated for an $L_{es} \times L_C$ area instead of its actual $L_S \times L_C$ area. The black-body radiation from each side is calculated for its actual $L_S \times L_C$ area with an effective emissivity of ϵ_W .

The schematic drawing **Figure 1b** (modeled on the flow patterns in Fujii and Imura [3] Fig. 14(e) and 14(f)) shows a plume rising from the center of an upward-facing plate fed by flow from the plate's edges. For the test surface, the upward heat flow of 0.467 W/K is more than twice the 0.212 W/K expected from the back and sides. Convective flow from the upward-facing test surface will draw in the air heated by the back and sides, reducing heat transfer from the test surface. In order to avoid double counting the convected heat from the back and sides, they should not be deducted from the plate heat (the thermal radiation is still deducted). The "reuptake" of this convected back and side heat should be nearly complete; its coefficient was set to 1 to avoid introducing another degree-of-freedom into the model.

Not deducting side convection from upward natural convection has an unexpected benefit: the upward convection model is thus insensitive to L_{es} , allowing ϵ_W to be determined from only upward-facing measurements.

XII. Radiative transfer side model

The 3 mm roughness plate had its sides wrapped with duck tape, which has a different emissivity from the foam wedges forming each side surface. Some of the 1 mm roughness plate runs were with tape and some without, requiring different ϵ_W values. For taped sides $\epsilon_W \approx 0.703$; without tape $\epsilon_W \approx 0.515$.

Figure C2a shows duck tape applied to the lower 54% of the plate's side, which corresponds to 50% coverage of the XPS foam wedge. For this partial tape coverage, ϵ_W Equation (C7) is the area proportional mean of the duck tape emissivity and XPS emissivity. Barreira et al. [21] measured ϵ_{dt} emissivities of 0.86 and 0.89 from two brands of "duck tape". The emissivity is largely

controlled by the exposed polyethylene film, and increases with oxidation. Hence, the larger value is used for the aged duck tape on the plate sides. As of this writing, published emissivity measurements of XPS foam have not been located.

$$\epsilon_W = 50\% \epsilon_{dt} + 50\% \epsilon_{XPS} \quad (C7)$$

Natural convection measurements ($u = 0$) from the plate assembly over the span of inclinations in **Figure 2** have less than 3.3% RMSRE when calculated with $\epsilon_{XPS} = 0.515$; the RMSRE increases to either side of 0.515. This value is consistent with natural convection measurements of the plate assembly without tape.

XIII. Natural convection side model

With ϵ_W thus determined, L_{es} was the remaining degree of freedom. Trials with vertical and downward plate measurements found that L_{es} had a value near the sum of the aluminum slab thickness 19.4 mm and the effective height of the side face of the roughness $\approx \sqrt{2}\epsilon$. This makes sense for a natural convection dimension; it is used for L_{es} . The 3 mm roughness plate has $L_{es} \approx 23.6$ mm; 1 mm has $L_{es} \approx 21.0$ mm.

In the vertical case, 1/2 of the heated air from the bottom side flows along the vertical test surface and would be counted twice. And 1/2 of the air drawn by the top side comes from the vertical test surface and would be counted twice. This vertical reuptake coefficient was set to 1/2; discrepancy from the actual reuptake coefficient will manifest as error in measurements.

Consider the (initially) vertical plate as θ decreases from 0° . As the bottom side face tilts upward, more (than half of the) heated air will rise toward the test surface. That heat will reduce the convection from the test surface. When tilted downward, the heat from the test surface will reduce the convection from the top side. To handle these cases, Equation (C8) includes a term $2 \cos \theta \sin \theta$ whose minimum of -1 is reached at $\theta = -45^\circ$ and a term $-2 \cos \theta \sin \theta$ whose minimum of -1 is reached at $\theta = +45^\circ$.

XIV. Combining radiative transfer and convection

A side's radiative emissions, U_ϵ , compete with its convective heat transfer. Both increase with side temperature, but both act to lower that side temperature. Competitive heat transfer processes can often be modeled using the ℓ^p -norm with $p > 1$. The value of p was adjusted so that the $\Delta T = 3.8\text{K}$ and $\Delta T = 11\text{K}$ data points align with the theory traces in **Figure 2**. The optimal range is between $p = 4/3$ and $p = 3/2$; the geometric mean of those values is $p = \sqrt{2}$. The $\ell^{\sqrt{2}}$ -norm appears three times in U_S Equation (C8).

Equation (C8) U_S is an amount which will be deducted from the measured heat flow. For each side, the $\ell^{\sqrt{2}}$ -norm of the radiative and convective conductances is paired with the product of the convective conductance and a continuous trigonometric function of θ which goes negative when the natural convection would otherwise be double counted. Because of the triangle inequality, the $\ell^{\sqrt{2}}$ -norm will be greater than the convective component; thus, each side's contribution to U_S will be positive.

No more than one reuptake process will be simultaneously active for a side. In Equation (C8) the expressions $\min(0, \sin \theta, -.5 \cos \theta, 2 \cos \theta \sin \theta)$ and $\min(0, \sin \theta, -.5 \cos \theta, -2 \cos \theta \sin \theta)$ return the negative of the largest magnitude potential reuptake. **Table C2** describes the natural convection parameters and function.

Note that this analysis applies only to the plate assembly in alignment with the wind-tunnel, and oriented to have at least one horizontal edge. Hence, rotation in plane of plate, ϕ , must be an integer multiple of 90° . The only effect of ϕ in the equations is to swap arguments L_F and L_W when ϕ is an odd multiple of 90° .

$$\begin{aligned} U_S = & \|U_\epsilon, U_N(\theta - 90^\circ, L_C, L_{es}, 0^\circ)\|_{\sqrt{2}} \\ & + U_N(\theta - 90^\circ, L_C, L_{es}, 0^\circ) \min(0, \sin \theta, -.5 \cos \theta, -2 \cos \theta \sin \theta) \\ & + \|U_\epsilon, U_N(90^\circ - \theta, L_C, L_{es}, 0^\circ)\|_{\sqrt{2}} \\ & + U_N(90^\circ - \theta, L_C, L_{es}, 0^\circ) \min(0, \sin \theta, -.5 \cos \theta, 2 \cos \theta \sin \theta) \\ & + 2 \|U_\epsilon, U_N(0^\circ, L_{es}, L_C, \theta)\|_{\sqrt{2}} \\ & + 2 U_N(0^\circ, L_{es}, L_C, \theta) \min(0, \sin \theta) \end{aligned} \quad (C8)$$

Table C2. Natural convection function and parameters.

Symbol	Description
$U_N(\theta, L_F, L_W, \phi)$	natural convective conductance from Jaffer [5]
θ	surface angle from vertical (-90° is face up)
L_F	plate length
L_W	plate width
ϕ	rotation in plane of plate; integer multiple of 90°
$L_C = 0.305$ m	plate length = side length
$L_S = 45.8$ mm	side width
$L_{es} = 19.4$ mm + $\sqrt{2} \epsilon$	effective side width for natural convection
$\epsilon_{wt} = 0.9$	wind-tunnel test chamber emissivity
$\epsilon_W \approx 0.703$ taped; 0.515 bare	effective side emissivity
h_R	black-body radiative surface conductance
$U_\epsilon = L_C L_S \epsilon_W \epsilon_{wt} h_R$	radiative emission from a side

U_{B0} is the test surface reuptake conductance from the back. Its $\min(0, \sin \theta)$ term is squared because the heated air from the back must flow around two right-angle edges to reach the test surface.

$$U_{B0} = -U_N(90^\circ, L_C, L_C, 0^\circ) \min(0, \sin \theta)^2 \tag{C9}$$

Figures C6–C8 show upward, vertical, and downward convection measurements, respectively. Taken from 3 mm and 1 mm roughness plates over a range of Ra values, these graphs, in combination with Figure 2 test the natural convection and radiative transfer side models.

The traces labeled “theory” are Equation (7) with the appropriate row of Table 2. The difference between $\psi = 0^\circ$ and $\psi = 180^\circ$ in Figure C7 is explained in Section 11.

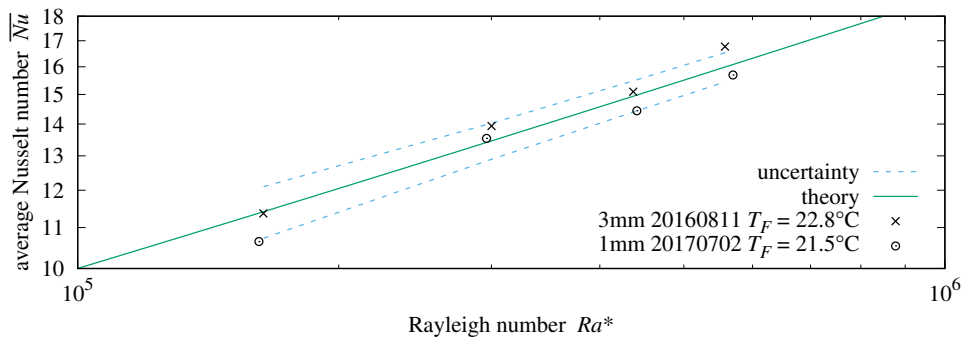


Figure C6. Natural convection from upward-facing surface.

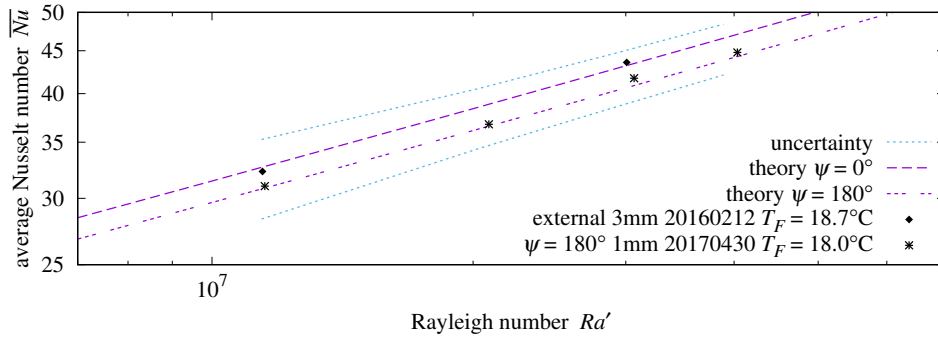


Figure C7. Natural convection from vertical surface.

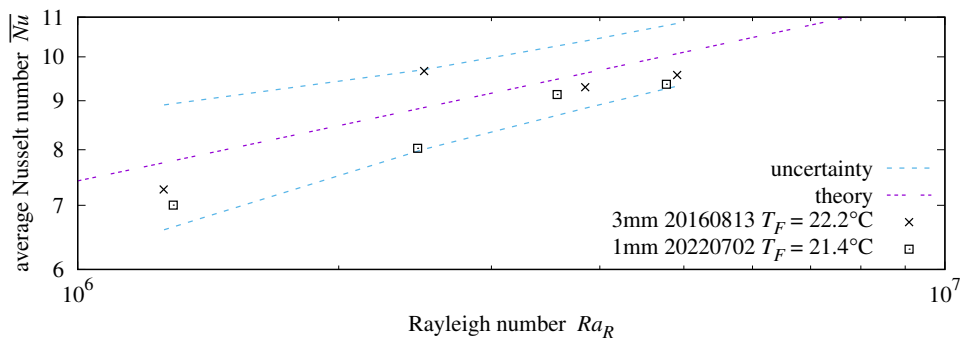


Figure C8. Natural convection from downward-facing surface.

XV. Mixed convection side model

Each $\ell^{\sqrt{2}}$ -norm instance of a call to U_N is replaced by a call to U_M , with first argument $U_{fl}(u)$ or $U_{ft}(u)$ **Table C3**. In order to ignore forced convection from the leading and trailing sides, $U_{ft}(u) = 0$ when $\psi = 90^\circ$ (horizontal flow); otherwise, $U_{fl}(u) = 0$. The reuptake instances of $U_N(\theta, L_F, L_W, \phi)$ are changed to the equivalent $U_M(0, \theta, L_F, L_W, \phi, 0^\circ)$.

Table C3. Mixed conductance functions and parameters.

Symbol	Description
$U_{fl}(u)$	level flow side forced thermal conductance
$U_{ft}(u)$	tilted flow side forced thermal conductance
u	bulk flow velocity
$U_M(U_F, \theta, L_F, L_W, \phi, \psi)$	mixed convective conductance
U_F	forced thermal conductance
θ	surface angle from vertical (-90° is face up)
L_F	forced characteristic length
L_W	other plate dimension
ϕ	rotation in plane of plate; integer multiple of 90°
ψ	angle of fluid flow from vertical (0° is upward)

$$\begin{aligned}
 U_S(u) = & \|U_\epsilon, U_M(U_{fl}(u), \theta - 90^\circ, L_C, L_{es}, 0^\circ, \psi)\|_{\sqrt{2}} \\
 & + U_M(0, \theta - 90^\circ, L_C, L_{es}, 0^\circ, 0^\circ) \min(0, \sin \theta, -.5 \cos \theta, -2 \cos \theta \sin \theta) \\
 & + \|U_\epsilon, U_M(U_{fl}(u), 90^\circ - \theta, L_C, L_{es}, 0^\circ, \psi)\|_{\sqrt{2}} \\
 & + U_M(0, 90^\circ - \theta, L_C, L_{es}, 0^\circ, 0^\circ) \min(0, \sin \theta, -.5 \cos \theta, 2 \cos \theta \sin \theta) \\
 & + 2 \|U_\epsilon, U_M(U_{ft}(u), 0^\circ, L_{es}, L_C, \theta, \psi)\|_{\sqrt{2}} \\
 & + 2 U_M(0, 0^\circ, L_{es}, L_C, \theta, 0^\circ) \min(0, \sin \theta)
 \end{aligned} \tag{C10}$$

When u is large, $U_S(u)$ approaches the sum of the forced convection conductances. $U_S(0) \equiv U_S$ of Equation (C8).

XVI. Measurement methodology

The measurement methodology employed is unusual. Instead of waiting until the plate reaches thermal equilibrium, the plate is heated to 15 K above ambient, heating stops, the fan runs at the designated speed, and convection cools the plate. All of the sensor readings are captured each second during the 102 min process, **Table C4** lists the dynamic physical quantities measured each second. **Table C5** lists computed quantities. Both $U_S(u)$ and $\{\epsilon_{Al} \epsilon_{wt} h_R A\}$ are subtracted from the combined heat flow. The mean of $\bar{h}(u, t)$ over the time interval in which ΔT drops by half (or exceeds 6142 s total time) is the result from that experiment.

Table C4. Dynamic quantities.

Symbol	Units	Description
ω	r/min	fan rotation rate
T_F	K	ambient air temperature
T_P	K	plate temperature
T_B	K	back surface temperature
P	Pa	atmospheric pressure
Φ	Pa/Pa	air relative humidity

Table C5. Computed quantities.

Symbol	Units	Description
h_R	W/(m ² K)	radiative surface conductance
$U_S(u)$	W/K	side radiative and convective conductance
$\bar{h}(u, t)$	W/(m ² K)	convective surface conductance

XVII. Heat balance

Collecting into $U_T(u)$ Equation (C11) those terms which have a factor of temperature difference $\overline{T_P} - \overline{T_F}$, Equation (C12) is the heat balance equation of the plate during convective cooling:

$$U_T(u) = U_S(u) + \{\bar{h}(u) A\} + \{\epsilon_{Al} \epsilon_{wt} h_R A\} \tag{C11}$$

$$0 = U_T(u) [\overline{T_P} - \overline{T_F}] + U_I [\overline{T_P} - \overline{T_B}] + C_{pt} \frac{d\overline{T_P}}{dt} \tag{C12}$$

The plate and ambient temperatures are functions of time t . Determined experimentally during heating, the temperature group-delay through the 2.54 cm block of insulation between the slab and back sheet is 110 s:

$$\overline{T_P}(t) = \frac{U_T(u) \overline{T_F}(t) + U_I \overline{T_B}(t - 110 \text{ s}) - C_{pt} [d\overline{T_P}(t)/dt]}{U_T(u) + U_I} \tag{C13}$$

To compute Nusselt number $\overline{Nu} = \overline{h} L/k$, Equation (C13) is solved for the $\{\overline{h}(u, t) A\}$ term from Equation (C11).

$$\varsigma(t) = -U_I [\overline{T_P}(t) - \overline{T_B}(t - 110 \text{ s})] \tag{C14}$$

$$\{\overline{h}(u, t) A\} = \frac{\varsigma(t) - C_{pt} [\overline{T_P}(t) - \overline{T_P}(t')]/[t - t']}{\overline{T_P}(t) - \overline{T_F}(t)} - \{\epsilon_{Al} \epsilon_{wt} h_R A\} - U_S(u) \tag{C15}$$

where t' is the previous value of t . In Equations (C14) and (C15), $\overline{T_P}(t)$, $\overline{T_F}(t)$, and $\overline{T_B}(t)$ are the 15-element cosine averages of plate and fluid temperatures (centered at time t).

In order to simulate T_P from the other dynamic inputs, (C13) is solved as a finite-difference equation where $dt = t - t' = 1$:

$$T_P(t) = \frac{U_T(u) \overline{T_F}(t) + U_I \overline{T_B}(t - 110 \text{ s}) + C_{pt} T_P(t')}{U_T(u) + U_I + C_{pt}} \tag{C16}$$

In Equation (C16), $T_P(t')$ is the previous simulated value, not a measured value.

XVIII. Measurement uncertainty

Following Abernethy et al. [22], the final steps in processing an experiment's data are:

- Using Equation (C15), calculate the sensitivities of convected power $\overline{h} A \Delta T$ per each parameter's average over the measurement time-interval;
- multiply the absolute value of each sensitivity by its estimated parameter bias to yield component uncertainties;
- calculate combined bias uncertainty as the root-sum-squared (RSS) of the component uncertainties;
- calculate the RSS combined measurement uncertainty as the RSS of the combined bias uncertainty and twice the product of the rotation rate sensitivity and variability.

Tables C6 and **C7** list the sensitivity, bias, and uncertainty for each component contributing more than 0.20% uncertainty for downward-facing 3 mm and 1 mm roughness plates, respectively. **Figure C9a, b** show the measurements relative to the present theory for rough flow and turbulent flow, respectively.

The supplementary data contains these graphs and tables for each data-set.

Table C6. Estimated measurement uncertainties, bi-level 3mm roughness at $Re = 59, 593$.

Symbol	Nominal	Sensitivity	Bias	Uncertainty	Component
ΔT	9.47K	+12.2%/K	0.10K	1.22%	LM35C differential
P	101kPa	+0.0009%/Pa	1.5kPa	1.28%	MPXH6115A6U air pressure
C_{pt}	4.69kJ/K	+0.024%/(J/K)	47J/K	1.13%	plate thermal capacity
η	0.401	+180%	0.014	2.52%	anemometer calibration
ς	6.00mm	+11285%/m	100um	1.13%	post height
				3.49%	combined bias uncertainty
Symbol	Nominal	Sensitivity	Variability	Uncertainty	Component
ω	905r/min	+0.081%/(r/min)	5.2r/min	0.43%	fan rotation rate
				3.60%	RSS combined uncertainty

Table C7. Estimated measurement uncertainties, bi-level 1mm roughness at $Re = 55,935$.

Symbol	Nominal	Sensitivity	Bias	Uncertainty	Component
ΔT	10.2K	+11.7%/K	0.10K	1.17%	LM35C differential
P	100.0kPa	+0.0008%/Pa	1.5kPa	1.26%	MPXH6115A6U air pressure
C_{pt}	4.24kJ/K	+0.028%/(J/K)	42J/K	1.17%	plate thermal capacity
η	0.340	+195%	0.003	0.66%	anemometer calibration
u_u	6.381	+2.44%	0.100	0.24%	diffuser airflow upper bound
L_T	8.34mm	+9365%/m	100um	0.94%	post length
L_m	3.57mm	+454%/m	500um	0.23%	side metal strip width
ϵ_{rs}	0.040	+20.4%	0.010	0.20%	test-surface emissivity
ϵ_{wt}	0.900	+9.05%	0.025	0.23%	wind-tunnel emissivity
				2.44%	combined bias uncertainty

Symbol	Nominal	Sensitivity	Variability	Uncertainty	Component
ω	1.03kr/min	+0.065%/(r/min)	2.5r/min	0.16%	fan rotation rate
				2.46%	RSS combined uncertainty

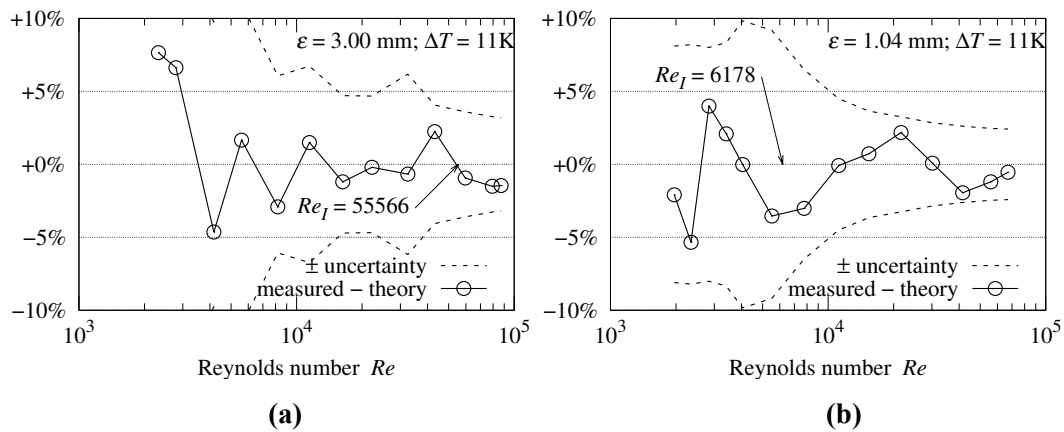


Figure C9. (a) Measured versus theory $\epsilon = 3$ mm and (b) Measured versus theory $\epsilon = 1$ mm.

XIX. Details

Documentation, photographs, electrical schematics, and software source-code for the apparatus, as well as calibration and measurement data are available from: <http://people.csail.mit.edu/jaffer/convect>.